Effects of Residual Water on Storage Canister Internal Components

Spent Fuel and Waste Disposition

Prepared for
U.S. Department of Energy
Spent Fuel and Waste Science and Technology

Pavan Shukla
Robert Sindelar

September 30, 2020

Milestone No. M3SF-20SR010207025
SRNL-STI-2020-00428

Prepared by
Savannah River National Laboratory
Savannah River Nuclear Solutions
Aiken, South Carolina 29808

Savannah River National Laboratory is a multiprogram laboratory managed and operated by Savannah River Nuclear Solutions, LLC, for the U.S. Department of Energy under contract DE-AC09-09SR22505.

EXECUTIVE SUMMARY

This report describes an evaluation of the spent nuclear fuel cladding and canister internal materials' corrosion/oxidation due to (inadvertent) residual free water inside a dry storage canister post-dryout. Drying of spent nuclear fuel (SNF) and the impact of (inadvertent) residual water in a SNF canister is being addressed under the DOE-NE Spent Fuel and Waste Science and Technology (SFWST) program to ensure the safe extended dry storage and transportation of commercial SNF.

A long-standing understanding has been that the amount of residual water in a storage canister after vacuum drying is not expected to be much more than trace amounts of 0.43 gram mole (NRC, 2010). However, recent findings from the High Burnup Demonstration project (Bryan et al., 2019a-c), and an Integrated Research Project (Knight, 2018) show that residual free water well above the amount of approximately 0.43 gm-moles that had been assumed for a 3 torr rebound pressure, may remain within an SNF canister following prototypic drying. In fact, an NRC-NMSS sponsored study considered residual water amount as high as 55 moles (CNWRA, 2013).

Considering the recent findings and the NRC-sponsored work, this present work was conducted to study the effects of unspecified amount of residual water on oxidation and corrosion of canister internals, i.e., it was assumed that the residual water amount is not limiting. It was assumed that the spent nuclear fuel content in the canister is not exposed to the internal environment, i.e., the packaged canister does not contain any damaged (breached) fuel.

The overall approach consisted of explicit accounting of both spatial and temporal variations of thermal conditions in a generic storage canister in the corrosion/oxidation of the materials. Radiolysis of the residual water is expected to result in the formation of hydrogen peroxide, both in liquid and vapor phase of the residual water. Literature information suggests that vapor phase hydrogen peroxide would decompose into oxygen and water; this reaction will be catalyzed by the cladding surface. On other hand, hydrogen peroxide in liquid water would persist. It was assumed that radiolysis would yield approximately 0.1 mole of hydrogen peroxide for each liter of residual water or 0.1 M concentration. Considering this, it was considered for the corrosion evaluation that hydrogen peroxide concentration in liquid phase residual water ranges between 0 to 2 M. Corrosion rates of various internal component materials were obtained as a function of temperature and hydrogen peroxide. Cladding materials' oxidation rates, reported in the previous study (Shukla, et al, 2019), were used. Additional analysis also indicated that cladding oxidation could only occur when temperatures are high enough for the residual water to be in vapor phase. Cladding oxidation rates and corrosion rates of the internal components were integrated with the spatial and temporal thermal conditions inside the canister for the storage period of 300 years. The specific components were those for the fuel cladding, fuel assembly components (spacer grids, guide tubes, water channels), fuel baskets, and neutron absorbing materials; details are provided in table below:

Table E-1. Listing of Various Internal Component Materials		
Components	**Materials**	**Notes**
Fuel rod claddings, guide tubes, and water channel	Zirconium based alloys Zircaloy-4, Zircaloy-2, ZIRLO and M5	Only Zircaloy-4, ZIRLO and M5 are considered in this work
Canister Shell and Lid, and fuel basket	300-series austenitic stainless steels, Type 304 and 304L	
Fuel basket	Predominantly used duplex and 300-series austenitic stainless steels, Type 304 Some vendors may have used Al fuel basket Carbon steel fuel basket in transfer canisters	Stainless steel guide tubes and carbon steel spacer materials are also used
Spacer grids	Zirconium based alloys Zircaloy-4, Zircaloy-2, ZIRLO and M5 Nickel-based alloys	None
Upper and lower end fittings	Zirconium based alloys 300-series stainless steel	None
Neutron absorbing material	Borated stainless steel Borated aluminum (BORAL™)	None

The assumptions were a load SNF in a generic composite canister with:

- 21 PWR assemblies with either Zry-4, ZIRLO, or M5 cladding, with total cladding surface area of approximately 600 m^2
- Canister internal cavity volume ≅ 12 m^3
- Fuel basket surface area ≅ 62.5 m^2
- Assembly hardware surface area ≅ 5 m^2
- Neutron absorbing plates' surface area ≅ 200 m^2

The corrosion/oxidation and related degradation phenomena included:

- General corrosion
- Localized corrosion including pitting, crevice, and galvanic corrosion

This study provided the following findings of corrosion/oxidation of the cladding and canister internals for the period of 300 years under decaying temperature conditions and with unlimited water:

- General corrosion is expected to be dominant degradation mechanism, localized corrosion either in form of pitting or crevice corrosion is unlikely.
- Maximum loss of cladding thickness due to general corrosion is not expected to exceed 13 μm. The maximum loss of cladding would occur for Zircaloy-4 in a canister with peak cladding temperature of 400 °C. The maximum cladding thickness loss will be confined to no more than 20 percent of the total fuel rods. The cladding thickness loss to the rods located away from the peak temperature of 400 °C is expected to be less than 3 μm. This material corrosion loss is effectively limited, regardless of the amount of residual water, due to the temperature drop-off in time with concomitant extremely low corrosion kinetics.

- Both stainless steel and nickel-based alloys and not expected to experience significant loss of thickness due to general corrosion. Maximum loss of thicknesses to the stainless steel and nickel-based components is expected to be on the order of 1 and 0.1 mm, respectively. This material corrosion loss is effectively limited, regardless of the amount of residual water, due to the temperature drop-off in time with concomitant extremely low corrosion kinetics.
- Corrosion of aluminum-based components could lead up to 0.4 mm loss of thickness. Most BORAL plates have sheathing layers of aluminum sheets which are 250-μm (0.25-mm) thick. This indicates that BORAL plates may experience extensive loss of thickness of aluminum sheathing where liquid phase residual water accumulates. The role of passive films that would reduce the corrosion rate of aluminum in the canister internal environment did not account for a complex oxide such as gibbsite/bayerite and boehmite mixtures.
- Corrosion of carbons-steel based components could be significant, and loss of thickness could exceed components' manufactured dimensions. However, carbon steel is not commonly used in the storage canisters, but may have been used in transportation canisters.

This present report complements the FY19 report "Consequence Analysis of Residual Water in a Storage Canister – Preliminary Report" N2SF-19SR010201055. That previous report looked at water partitioning, pro-rated to temperature-dependent oxidation kinetics for the materials system and included exposed fuel.

This present report fulfills the M3 milestone M3SF-20SR010207025 under Work Package Number SF-20SR01020702.

References

Bryan, C.R., S.G. Durbin, E. Lindgren, A.G. Ilgen, T.J. Montoya, T. Dewers, D. Fascitelli. "SNL Contribution: Consequence Analysis for Moisture Remaining in Dry Storage Canisters After Drying," Sandia National Laboratory, SAND2019-8532 R, 2019a.

Bryan, C.R., R.L. Jarek, C. Flores, and E. Leonard. Analysis of Gas Samples Taken from the High Burnup Demonstration Cask. SAND2019-2281. Sandia National Laboratories, Albuquerque, NM. 2019b.

Bryan, C., R.L. Jarek, C. Flores, and E. Leonard. "Analysis of Gas Samples Collected from the DOE High Burnup Demonstration Cask". International High-Level Radioactive Waste Management Conference 2019. Knoxville, TN, American Nuclear Society. 2019c.

CNWRA. Extended Storage and Transportation: Evaluation of Drying Adequacy. Authors: H. Jung, P. Shukla, T. Ahn, L. Tipton, K. Das, X. He, and D. Basu, San Antonio, Texas: Center for Nuclear Waste Regulatory Analyses. 2013.

Knight, T. "Experimental Determination and Modeling of Used Fuel Drying by Vacuum and Gas Circulation for Dry Cask Storage," Nuclear Energy University Program, Project No. 14-7730. U.S. Department of Energy, 2018.

NRC. NUREG–1536, "Standard Review Plan for Spent Fuel Dry Storage Systems at a General License Facility." Rev 1. Washington, DC: U.S. Nuclear Regulatory Commission. 2010.

Shukla, P., R. Sindelar, P.-S. Lam "Consequence Analysis of Residual Water in a Storage Canister." SRNL-STI-2019-00495. Aiken, South Carolina: Savannah River National Laboratory. 2019.

TABLE OF CONTENTS

LIST OF FIGURES

LIST OF TABLES

ACRONYMS

BWR	Boiling Water Reactor
CNWRA	Center for Nuclear Waste Regulatory Analysis
DOE	US Department of Energy
HBU	High Burn-Up
IRP	Integrated Research Project (type of NEUP)
LWR	Light Water Reactor
NE	Nuclear Energy
NEUP	Nuclear Energy University Program
NRC	Nuclear Regulatory Commission
NMSS	Nuclear Material Safety and Safeguards
PWR	Pressurized Water Reactor
PNNL	Pacific Northwest National Laboratory
RH	Relative Humidity
SFWD	Spent Fuel and Waste Disposition
SNF	Spent Nuclear Fuel
SNL	Sandia National Laboratories
SRNL	Savannah River National Laboratory

This page intentionally left blank.

1. INTRODUCTION

Drying of spent nuclear fuel (SNF) and the impact of (inadvertent) residual water in a SNF canister, identified as a high-priority gap, is being addressed under the DOE-NE Spent Fuel and Waste Science and Technology (SFWST) program to ensure the safe extended dry storage and transportation of commercial SNF (Teague et al., 2019). This report is part of the investigation to characterize the impact of residual water, post-dry out.

The U.S. Nuclear Regulatory Commission (NRC), Office of Nuclear Material Safety and Safeguards (NMSS) had recognized that inadvertent free water could remain in SNF casks/canisters, and sponsored a study in 2012 to investigate the impact of that water on the SNF and canister internal materials. The study considered residual water amount as high as 55 moles (CNWRA, 2013). A report under the SFWST program prepared in 2019 updated and refined the corrosion/oxidation models used in the NRC work (Shukla, et al, 2019). Both of those studies did not explicitly look at the corrosion of non-fuel canister internals. Recent work (Bryan et al., 2019a-c; Knight et al., 2017; Knight, 2017) indeed showed that inadvertent free water (>> 0.43 moles or approximately 8 ml, Knoll, et al, 1987) may remain within the SNF canister following drying even with a dryness criterion of 3 torr pressure limit following a 30-minute hold after active drying is completed.

This present investigation evaluates the effects of unspecified (unlimited) amount of the residual water on oxidation of fuel cladding and corrosion of canister internals such as fuel basket, neutron absorbing materials, and various assembly hardware as separate material systems for a 300-year period. It was further assumed that the spent nuclear fuel content in the canister is not exposed to the internal environment, i.e., the packaged canister does not contain any damaged (breached) fuel. Further, partitioning or pro-rating of a finite amount of water between the set of materials of the fuel and canister internals based on corrosion kinetics of the respective materials was not performed.

The overall all approach consisted of explicit accounting of both spatial and temporal variations of thermal conditions in a generic storage canister in the corrosion/oxidation of the materials. Radiolysis of the residual water is expected to result in the formation of hydrogen peroxide, both in liquid and vapor phase of the residual water. Literature information suggests that vapor phase hydrogen peroxide would decompose into oxygen and water; this reaction will be catalyzed by the cladding surface. On other hand, hydrogen peroxide in liquid water would persist. The details of the analysis and the results are reported.

2. OBJECTIVE AND SCOPE

The objective of this work is to examine the effects of an unspecified (unlimited) amount of residual water on oxidation of fuel cladding and corrosion of canister internals. Residual water may remain in SNF dry storage canisters after the fuel assemblies are transferred to the canister in the spent fuel pool (SFP), the canister is removed from the SFP and drained or pumped, vacuum dried in several pressure reducing steps, and backfilled with helium. This residual water from incomplete drying could degrade fuel rod cladding and cause corrosion of canister internals. Specifically, if residual water content is high enough, it could corrode internal components inside the canister, e.g., fuel basket, and neutron absorber plates. Considering this, focus of this work to determine extent of cladding oxidation and corrosion of canister internals due to unspecified (unlimited) amount of residual water. Residual water will decompose by radiolysis and create reactive oxidizing species such as oxygen and H_2O_2, which, at sufficient high temperatures will oxidize cladding, and in aqueous phase cause corrosion of canister internals.

The report describes an evaluation of the potential cladding oxidation and canister internal corrosion due to the residual water. An integrated quantitative approach was used to estimate the effects. The approach consisted of (i) the temporal and spatial evolution of thermal conditions in the cask, and (ii) the physicochemical processes that affect degradation of the materials within the cask. Regarding (ii), cladding oxidation in oxidizing environment, and corrosion of canister internals in aqueous phase environments were considered. Canisters are pressurized with 2 atm of helium. Vapor pressure of water is approximately 2 atm at 120 °C. For this reason, aqueous corrosion of canister internal components was considered below 120 °C. The canister internal components and cladding oxidation mass action equations are modeled in five time-dependent distinct temperature zones inside the cask's internal volume. A CASTOR V/21 cask was selected for defining five temperature zones to track thermal evolution in a storage canister. For each zone, the cladding and canister internals' surface areas were exposed to oxidizing environments, and corresponding oxidation and corrosion extents were calculated. The storage timespan of 300 years was subdivided into small enough increments such that thermal variations were within 1 °C within a time increment in all five zones. The calculation sequence was continued for the storage tie of 300 years. Detailed descriptions of the critical steps involved are described in Chapter 3, followed by simulation data and results of the integrated analysis in Section 4. Summary, conclusions, and future refinements are discussed in Chapter 5, and references cited in this work are listed in Chapter 6.

3. TECHNICAL APPROACH

3.1 Internal Materials

Zirconium Alloys and Spend Nuclear Fuel

Zircaloy-4, Zircaloy-2, ZIRLO and M5 have been widely used to fabricate the fuel claddings. The alloys are also used for the guide tubes and water channels in the fuel assemblies. The alloys are also often used for assembly components such as spacer grids. Zircaloy-4, ZIRLO and M5 are considered for corrosion analysis in this report.

Spent nuclear fuel oxidation is not considered in this report because the fuel is assumed to be not exposed to the canister internal environment.

Carbon Steel

Carbon steel fuel basket is used in the transportation canisters. Some canisters used for transportation may also have been used for storage.

Stainless Steel

300-series austenitic stainless steels are predominantly used in constructing DSS subcomponents. Type 304 and 304L are widely used, however, some venders may have used other variations of this stainless steel. Some vendors have also used 304L for assembly hardware components. The canister components made of stainless steel include canister shell, lid, fuel basket, and fuel assembly components such as lower and upper end fittings and poison rod assemblies in PWR.

Aluminum Alloys

In DSSs, aluminum and its 6000 series alloys are commonly used inside the system to transfer heat because of their good thermal conductivity. Aluminum is also used for fabrication of the BORAL plates. Some vendors may have used the aluminum fuel basket in the storage canisters.

Nickel Alloys

Nickel-based alloys are used for assembly components. The assembly hardware considered here includes spacer grids, and lower and upper end fittings. The other components are fabricated using one of the following materials: Inconel 718, Inconel 625, Inconel X-750.

Borated Stainless Steel

Borated stainless steel is used inside the DSS as one type of neutron-absorbing material exposed to helium and residual water. Type 304 borated stainless steels are similar in composition to nominal Type 304 stainless steels except that they contain boron, which provides a much higher thermal neutron absorption cross-section. ASTM A887–89 defines eight types of borated stainless steels (304B and 304B1–304B7) with boron concentrations from 0.2 to 2.25 weight percent (ASTM International, 2009).

Under a neutron flux, Boron-10 nuclei capture neutrons, yielding Boron-11 nuclei, which decay into alpha particles and Lithium-7, i.e., one neutron depletes one Boron-10. Borated stainless steel typically contains 10^{19} to 10^{21} Boron-10 atoms/cm^2 (EPRI, 2009). Although small fraction of boron alloy with

stainless steel, the boron density can reach this level by adjusting the thickness of the absorber, by adjusting the weight fraction of added boron, and through the use of enriched boron (i.e., Boron-10) (EPRI, 2009). A neutron flux of 10^4–10^6 n/cm^2-s is typical for dry cask storage (Sindelar et al., 2011). At a typical neutron flux and Boron-10 concentrations, the neutron dose after 60 years would deplete at most 0.0002 percent of the available Boron-10 atoms. Using the highest expected neutron flux and the lowest Boron-10 concentration as a most conservative scenario, only 0.1 percent of the available Boron-10 atoms would be depleted after 300 years, an amount too small to decrease any criticality control function of the neutron absorbing materials.

Borated Aluminum Alloys and Aluminum-Based Composites

Commonly used neutron absorbers include borated aluminum alloys, aluminum metal matrix composites, such as Metamic™ and Boralyn®, and aluminum-boron carbide laminate composites, commonly referred to as cermets, such as Boral®. Like borated stainless steel, loss of boron is expected to not affect the criticality control. Various components and materials are listed in Table 3-1.

Table 3-1. List of Various Internal Components and Materials

Components	Materials	Notes
Fuel rod claddings, guide tubes, and water channel	Zirconium based alloys Zircaloy-4, Zircaloy-2, ZIRLO and M5	Only Zircaloy-4, ZIRLO and M5 are considered in this work
Canister Shell and Lid, and fuel basket	300-series austenitic stainless steels, Type 304 and 304L	
Fuel basket	Predominantly used duplex and 300-series austenitic stainless steels, Type 304 Some vendors may have used Al fuel basket Carbon steel fuel basket in transfer canisters	Stainless steel guide tubes and carbon steel spacer materials are also used
Spacer grids	Zirconium based alloys Zircaloy-4, Zircaloy-2, ZIRLO and M5 Nickel-based alloys	None
Upper and lower end fittings	Zirconium based alloys 300-series stainless steel	None
Neutron absorbing material	Borated stainless steel Borated aluminum	None

3.2 Corrosion Mechanisms

Presence of residual water is most likely could result in general, localized, and galvanic corrosion of the internal structural components; these electrochemistry-based corrosion mechanisms are considered in this

work. The electrochemistry-based corrosion mechanisms are expected to be dominant when residual water is in liquid phase which is possible when temperature is below 120 °C. In addition to the electrochemistry-based corrosion mechanisms, oxidation of the cladding materials in also considered. A list of various corrosion mechanisms, mechanisms' description and potentially affected components is provided in Table 3-2.

Table 3-2. Corrosion Mechanisms with Potentials to Affect the Internal Components

Mechanisms	Description	Notes
General Corrosion	General corrosion is characterized as a uniform surface loss of the component, and involves oxidation and reduction reactions at the interface of the metal and electrolyte.	Considered for all the components, but not the humid air corrosion because of helium rich environment.
Localized corrosion in form of Pitting Corrosion	Pitting corrosion depends on development of a localized environment. Pitting corrosion results from breakdown of the oxide film at inhomogeneous structures, such as precipitates, or at grain boundaries where the oxide film may be less protective. Once the oxide film breaks down, pit growth can occur and an aggressive environment can form in the pit, thus sustaining the pit growth.	Considered for all the components
Localized corrosion in form of Crevice Corrosion	This degradation mechanism is associated with conditions where there are two components in close proximity that creates a crevice. Inside a crevice, a stagnant environment forms that allows the chemistry to become more aggressive than in the bulk environment.	Criterion for the pitting corrosion applied to screen the crevice corrosion.
Galvanic Corrosion	Galvanic corrosion is caused when two materials of different corrosion potential are in electrical contact with same electrolyte. The corrosion rate of the more active material will increase as a result of this interaction. The increased corrosion rate depends on the relative area for the two materials and the difference between the corrosion potentials. Galvanic corrosion may increase the general corrosion rate or lead to localized corrosion, such as pitting or crevice corrosion.	This mechanism is situation dependent. An analysis is conducted.
Stress Corrosion Cracking	SCC is an environmentally induced cracking mechanism that is produced in a susceptible material by the combined effect of having an aggressive environment and tensile	Based on NRC (2019), this mechanism is unlikely.to

Table 3-2. Corrosion Mechanisms with Potentials to Affect the Internal Components		
Mechanisms	**Description**	**Notes**
	stress. SCC is highly dependent on the specific chemical environment and material composition.	affect the components.
Microbiologically Influenced Corrosion	This type of degradation can occur when biological activity is present in the form of various bacteria or fungi. Bacteria or fungi ingest nutrients and alter the local environment that promotes corrosion.	This mechanism is unlikely because high-level of radiations will suppress any biological activity.
High Temperature Air Oxidation	This form of degradation occurs as metals exposed to dry air at high temperatures react with oxygen, forming an oxide layer.	Considered for zirconium alloys.
Hydrogen Embrittlement	A degradation mechanism can occur in high strength materials. Hydrogen may be absorbed into the material, which can reduce the material toughness. The hydrogen can be natural to the environment, formed by corrosion processes, or formed by water dissociated through radiolysis.	NRC (2019) discussed this mechanism for various zirconium-based alloys.
Blister Formation/Expansion	Blister formation is a degradation mechanism that has been observed in the cladding of BORAL, which has been used in both BWR and PWR fuel assembly storage since 1964. The blisters are characterized by a local area where the aluminum cladding separates from the underlying boron carbide–aluminum composite, and the cladding is physically deformed outward.	Considered for BORAL
High Temperature Steam Oxidation	This form of degradation occurs as metals react with high temperature steam forming a relatively thick oxide layer.	Cladding oxidation rates are that for the canister internal conditions, based on literature information. This mechanism for other component materials was not considered.

3.3 Fuel and Cladding Temperatures

The fuel and cladding temperatures are expected to vary in the storage space of the canister. If a canister is loaded with fuel assemblies with equal decay heat, the fuel and cladding temperature are expected to be maximum near center of a canister, otherwise, fuel and cladding temperature will be a complex function of each assembly decay heat and other related parameters. For the sake of simplicity, it is assumed that a storage canister is loaded with fuel assemblies with near equal decay heat, and maximum temperature occurs near the center of the canister. Recent work on modeling storage temperature of the high burnup fuel assemblies indicate peak temperature near 325 °C (Jensen and Richmond, 2019), however, there is no certainty that peak temperature will not be near 400 °C if utilities decide to store hotter fuel assemblies than the ones considered in Jensen and Richmond (2019). In addition, discussion with NRC staff indicated that the estimated peak temperature could have error of ±20 °C; therefore, it is assumed that zone peak cladding temperature is 400 °C for a limiting case, and 302 °C for a nominal case.

The fuel and cladding temperatures are expected to vary both temporarily and spatially. The temporal variations were modeled using an exponential decay function (McKinnon et al., 1992). The time-dependent fuel and cladding temperature $T(t)$ is given by Eq. (3–1)

$$T(t) = (T_{init} - 309)\exp(-at) + 309 \qquad (3–1)$$

where T_{init} is the initial fuel and cladding temperature (K), and a is a thermal decay constant. The value of the decay constant (a) is either 0.023 or 0.064. A zone approach was used to model spatial variation of the fuel and cladding temperature; the approach is the same as the one used in CNWRA (2013). A short description is provided. Temperature distribution in a fuel basket loaded with 21 fuel assemblies with equal decay heats is presented in Figure 3–1; the distribution depiction is only for a quarter of the basket. As seen in the figure, the temperature varies spatially through the basket. The basket is divided into five temperature zones, as shown in Figure 3–2, to easily track the temperature distribution and its temporal variation. The fuel and cladding temperature in each zone is assigned a mean value, which is the average of the maximum and minimum temperatures in the zone. Various zone mean temperatures are listed in Table 3-3. The temporal variation in temperature in each zone is calculated using Eq. (3–1); T_{init} is replaced by mean value of the temperature in each zone denoted by T_{mean} and listed in Table 3-3.

Table 3-3. Mean Temperatures T_{mean} in Eq. (3–1) and Percentage of Volume of Five Temperature Zones

Zone Number	Fuel and cladding initial temperature K (°C) with peak temperature of 302 °C	Fuel and cladding initial temperature K (°C) with peak value of 400 °C	Percentage of total volume of fuel basket
1	575 (302)	673 (400.0)	18.95
2	525 (252)	623 (350.0)	33.00
3	475 (202)	573 (300.0)	33.72
4	425 (152)	523 (250.0)	12.38
5	375 (102)	481 (208.0)	1.95

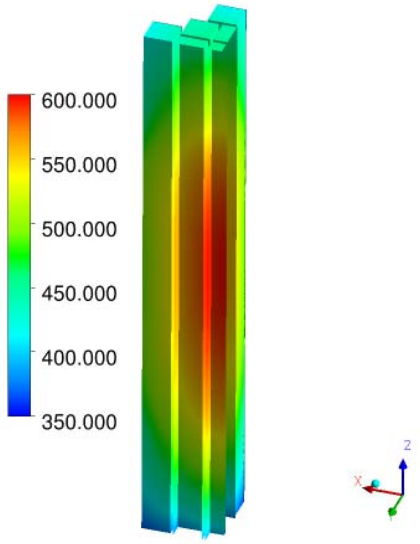

Figure 3–1. Temperature (K) Distribution in CASTOR V/21 Fuel Basket Assembly (CNWRA, 2013).

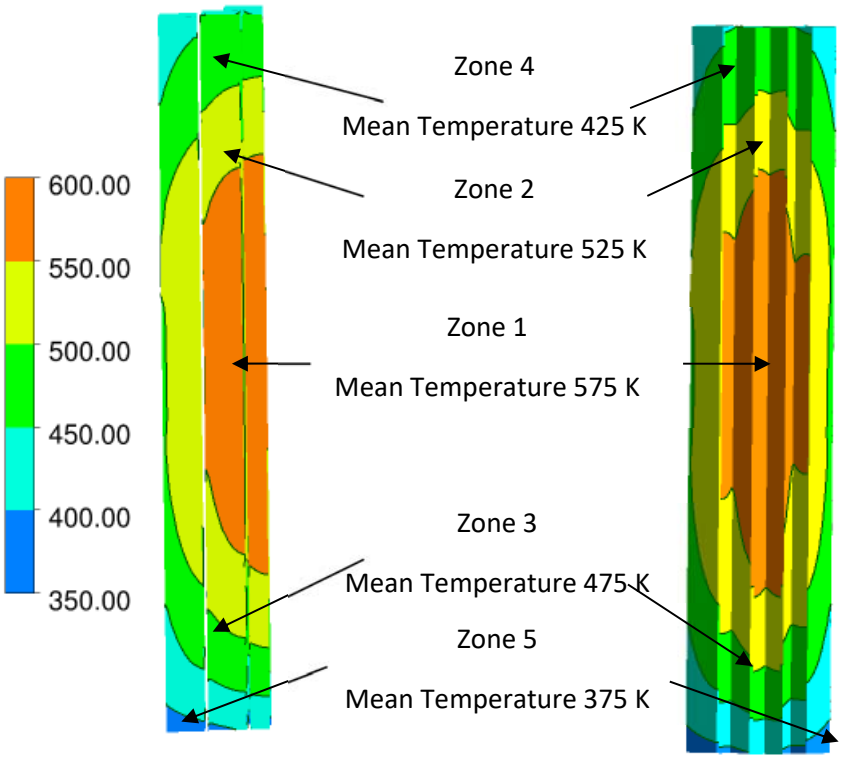

Figure 3–2. Location of the Five Temperature Zones in CASTOR V/21 Fuel Basket Assembly (CNWRA, 2013)

3.4 Radiolysis of Residual Water

A topical report on the radiolysis of residual water estimated for the HBU Demo was recently reported (d'Entremont et al., 2020). The residual waters, post-dry-out subject to radiolysis included:

- free water trapped as a liquid and/or water as a vapor;
- physisorbed/chemisorbed water that is bound to internal surfaces, such as the cask and internals including fuel rods and aluminum components. This water is bound with varying adsorption energy, typically with the first few monolayers strongly bound with weakly bound layers forming on top in equilibrium with the humidity; and
- chemisorbed water on internal surface films that is chemically-bound in an (oxy)hydroxide.

The free and physisorbed waters radiolytically breakdown into molecular hydrogen and hydrogen peroxide, an oxidizing specie, that itself would decompose into hydrogen and oxygen, with the oxygen expected to be reacted with zirconium fuel cladding, resulting in net generation of hydrogen gas. Radiolytic breakdown of chemically-bound water in (oxy)hydroxides can also occur to generate hydrogen gas.

CNWRA (2013) work assumed the hydrogen peroxide would be decomposed into hydrogen and oxygen, and that the oxygen would be consumed by the zirconium materials in the cask. The hydrogen generation in that report is consistent with this present report that looks at the corrosion/oxidation from free water. CNWRA (2013) radiolysis model was for decomposition of the water in vapor phase, and back reactions were not considered to be dominant because of direct reaction between radiolytic products and cladding; as a result, the radiolysis kinetic equilibrium will shift towards the products, and thus, minimize incidents of the back reactions.

This work is predominantly focused on electrochemistry-based corrosion of canister internals in liquid phase water. Buxton et al (1988) proposed following chemical reactions for radiolysis of the water:

$$H_2O \rightsquigarrow [0.28]OH^{\bullet} + [0.06]H^{\bullet} + [0.27]e^{-}_{aq-} + [0.05]H_2 + [0.07]H_2O_2 + [0.27]H^{+}_{aq} \quad (3\text{–}2)$$

where concentration in the bracket are the radiolytic yields of deposited energy. It is clear from the above equation that H_2O_2 is the key oxidant that will persist in the liquid phase water; vapor phase hydrogen peroxide is expected to decompose into oxygen and water, catalyzed by the cladding surface with oxides (Lousada and Jonsson, 2010). Kinetic rates of the radiolysis reaction are not fully understood in a storage canister conditions and require additional research. Considering this lack of understanding and uncertainty, it is assumed that H_2O_2 concentration ranges from 0 to 2 M in the liquid phase water that might persist in a storage canister.

3.5 Cladding Oxidation and Corrosion Kinetics

There are two potential pathways for cladding oxidation due to residual water in dry storage: (i) water radiolysis products (i.e., oxygen and highly oxidizing species such as $OH^{\bullet}$ or H_2O_2) present in the canister can react with zirconium cladding to form zirconium oxide on the exposed cladding surfaces, (ii). cladding directly reacting with water molecules. Regarding (i), Suzuki and Kawasaki (1986) proposed following oxidation kinetics for Zircaloy-4 in air:

$$\Delta W\ (Zirc-4)\ = At \exp\left(-Q/\mathrm{R}T\right) \quad (3\text{–}3)$$

where

$\Delta W\ (Zirc-4)$	—	weight gain (g/m^2) for Zircaloy-4
A	—	preexponential constant (g/m^2/hr) = 3.25 × 10^5
t	—	time (hr)
Q	—	activation energy (J/mol) = 1.13 × 10^5
R	—	gas constant (J/mol/K) = 8.314
T	—	absolute temperature (K)

Oxidation rate data for ZIRLO™ and M5™ in the dry storage temperature range could not be found. Argonne National Laboratory (NUREG/CR-6846) conducted a study to estimate oxidation rates of steam-preoxidized Zircaloy-4, ZIRLO and M5 samples exposed to dry air at various temperatures. ANL rate constantans are applicable above 400 °C; the ANL data at and below 400 °C showed negligible mass gain in the samples exposed to the oxidation conditions. ANL used the data to estimate pre-exponential constant and *Q/R*; these two parameters are listed in Table 3-4. The rate constant estimated from the ANL data are for the oxidation growth phases of pre-breakaway and post-breakaway kinetics. Overall oxide growth phase can be divided in two periods: pre-breakaway and post-breakaway, as illustrated in Figure 3–3; initially a cyclic pre-breakaway period occurs in which initial parabolic growth is followed by kinetic transition into post-breakaway with accelerated corrosion and a new parabolic growth cycle. The rate constants for the pre-breakaway and post-breakaway oxide growth phases of Zircaloy-4, ZIRLO, and M5 are shown in Figure 3–4(a), Figure 3–4 (b), and Figure 3–4(c), respectively.

Oxidation rates for ZIRLO and M5 were estimated using the following expression

$$\Delta W\ (ZIRLO)\ = At\ \exp\left(-Q/\mathrm{R}T\right) \times \frac{k_{ZIRLO,ANL}}{k_{ZIRC-4,ANL}} \tag{3–4}$$

and

$$\Delta W\ (M5)\ = At\ \exp\left(-Q/\mathrm{R}T\right) \times \frac{k_{M5,ANL}}{k_{ZIRC-4,ANL}} \tag{3–5}$$

where

$\Delta W\ (ZIRLO)$	—	weight gain (g/m^2) for ZIRLO
$\Delta W\ (M5)$	—	weight gain (g/m^2) for M5
$k_{ZIRC-4,ANL}$	—	Rate constant (kg^2/m^4/sec) for Zircaloy-4 based on ANL work
$k_{ZIRLO,ANL}$	—	Rate constant (kg^2/m^4/sec) for ZIRLO based on ANL work
$k_{M5,ANL}$	—	Rate constant (kg^2/m^4/sec) for M5 based on ANL work

It has been generally observed that the peak oxide thickness of Zircaloy-4 increased as the burnup increased up to approximately 75 GW-day/MTU (Garde, 1991; Van Swam, et al., 1997; EPRI, 2007); measurements of more than 4,400 commercial fuel rods irradiated in reactors worldwide show that the average oxide thickness on Zircaloy-4 was up to 100 μm for burnups in the range of 60–65 GW-day/MTU (EPRI, 2007). At low burnup (<45 GW-day/MTU), the average oxide thickness was 40 μm. Considering extent of oxidation of Zircaloy-4 during reactor operations and rate constants of pre- and post-breakaway phases, rate constant of the post-breakaway phase was used in Eqs. (3–4) and (3–5).

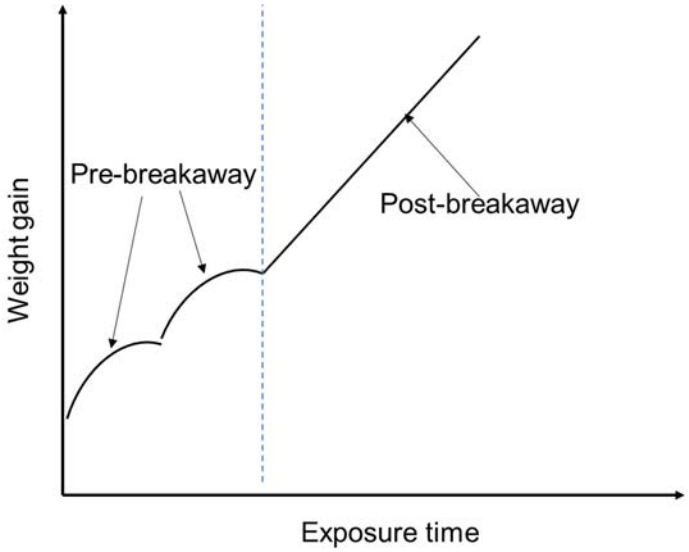

Figure 3–3. Schematic Representation of Pre-Breakaway and Post-Breakaway Oxide Growth Phases on Zr-Based Cladding Alloys

Compared to Zircaloy-4 cladding, oxidation data for new alloys are still lacking to confirm the range of oxide thickness at the high burnup regime (Cheng et al., 2000). However, for ZIRLO rods having an average burnup of 52.5 GW-day/MTU, the average peak oxide thickness for ZIRLO was 31 μm, which is approximately 27.5 percent of the average oxide thickness for conventional Zircaloy-4 (Sabol, et al., 1994). Considering that ZIRLO oxidation extent is smaller than Zircaloy-4, but the oxidation regime in dry storage is likely to be post-breakaway, post-breakaway rate constant values in Eq. (3–4) were used.

Data for M5 indicate that the oxide layer thickness is expected to range between 10 to 30 μm in 30 to 55 GW-day/MTU burnup range (Mardon et al, 2000). The pre-breakaway rate constant for M5 is an order of magnitude higher than the post-breakaway constant below 400 °C, as in Figure 3–4 (c). Considering that oxide growth during dry storage is expected to be post-breakaway phase, the post-breakaway rate constant values in Eq. (3–5) were used. Zircaloy-4 rate constant from Suzuki and Kawasaki (1986), and ZIRLO and M5 rate constants in Eqs. (3–4) and (3–5), respectively, are presented in Figure 3–5.

Table 3-4. Values of Preexponential Constant and Ratio of Activation Energy to Gas Constant for Zircaloy-4, ZIRLO, and M5

Cladding alloy	Oxide growth phase	Preexponential constant A ($kg^2/m^4/sec$)	Ratio of activation energy and gas constant Q/R (K)
Zircaloy-4	Pre-breakaway	0.386	16070
	Post-breakaway	187.3	19245
ZIRLO	Pre-breakaway	0.86	16100
	Post-breakaway	1.72×10^4	22865
M5	Pre-breakaway	1.0×10^{-3}	12230
	Post-breakaway	1.3×10^5	25290

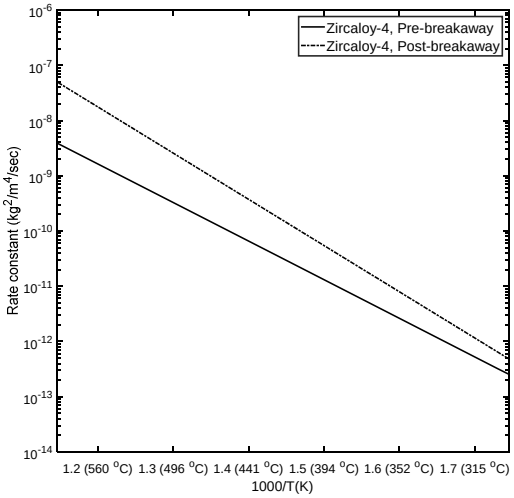

(a) Zircaloy-4

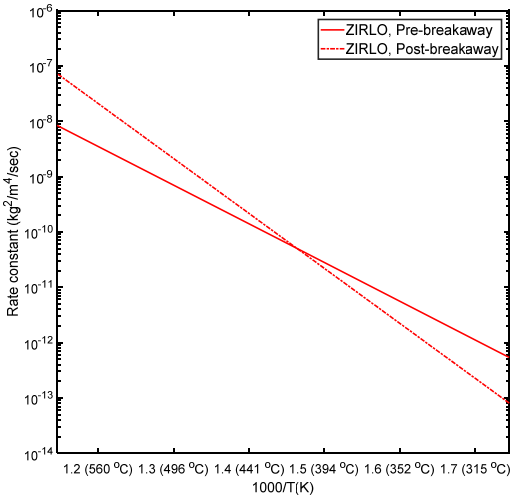

(b) ZIRLO

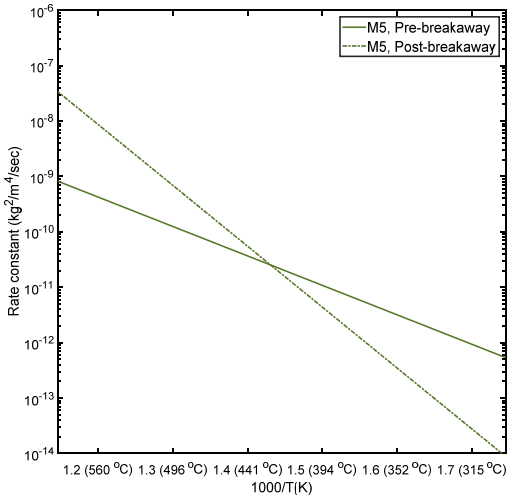

(c) M5

Figure 3–4. Rate Constant as a Function of Temperature for (a) Zircaloy-4, (b) ZIRLO, and (c) M5 in Temperature Range of 300 to 600 °C

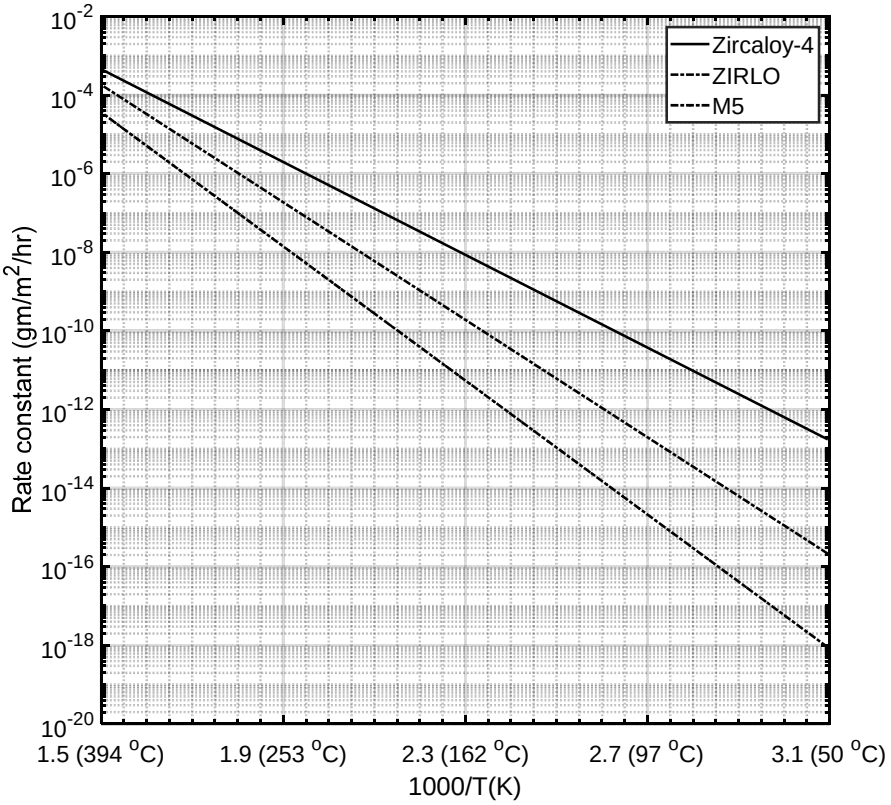

Figure 3–5. Rate Constant versus Temperature for Zircaloy-4, ZIRLO, and M5 in Dry Storage Temperature Range

A direct reaction between water and zirconium would occur when water contacting the cladding material is either in the liquid phase or the RH is above a threshold value and the cladding temperature is sufficiently high (CNWRA, 2013). The threshold RH value is assumed to be 20 percent based on the similarity in thermodynamic and near equal nobility between zirconium and aluminum. For aluminum cladding, the minimum RH required to sustain detectable oxidation is approximately 20 percent at 150 °C. Because aluminum and zirconium have been shown to have a similar thermodynamic and practical nobility based on Pourbaix classification of the nobility order (Ghali, 2010) and exhibit a similar corrosion performance with the formation of a protective oxide film, a threshold RH of 20 percent can also be assumed for zirconium-based cladding materials.

When water is in liquid phase, cladding materials can react with the water and result in additional cladding thickness. An analysis was conducted to estimate the extent of cladding oxidation as a function of temperature when water directly reacts with liquid phase water. A list of cladding oxidation models was compiled in CNWRA (2013). The oxidation rate of cladding materials has a strong positive dependence on temperature. Corrosion of zirconium and its alloys—in particular, Zircaloy-2 and Zircaloy-4—has been extensively studied in water and steam, and a large database exists as a result of the broad experience with LWRs (Cox, 1988, 1976; Rothman, 1984; Hillner, et al., 1994). Because most experiment data regarding cladding oxidation rate is for Zircaloy-4, the cladding oxidation assessment in this study is based on Zircaloy-4. Hillner, et al. (1994) conducted detailed analysis of weight measurement data from long-term autoclave tests of Zircaloy-2 and Zircaloy-4. The tests were conducted in degassed pure water for 10,507 days at temperatures ranging between 250 and 360 °C. Twenty-two different tests were analyzed, and specimens with different heat treatment and preoxidized surface conditions were included. Based on their data, Hillner, et al. (1994) proposed the reaction kinetics in the

form of Eq. (3–3). A number of other investigators also conducted similar oxidation tests in autoclaves and established their own values in terms of activation energy and preexponential constants, listed in Table 3-5.

Table 3-5. Zircaloy Cladding Oxidation Rate Constants A and Q/R in Eq. (3–3) for from Various Sources

Model No.	Investigators*	A (mg/dm^2/day)	Q/R (K)
1	Hillner (1977)	1.12×10^8	12,529
2	Van der Linde (1965)	2.30×10^9	14,451
3	Dyce (1964)	6.53×10^9	15,109
4	Daalgard (1976)	1.84×10^7	11,222
5	Billot, et al. (1989)	1.13×10^8	12,567
6	Garzaolli, et al. (1982)	1.18×10^9	13,815
7	Stehle, et al. (1975)	2.21×10^9	14,242
8	Peters (1984)	8.12×10^8	13,512
9	Hillner, et al. (1994)	2.46×10^8	12,877

*Full citations are listed in the reference section.

The listed models in Table 3-5 were exercised for the temperature-time profile in Figure 3–6; the temperature profile is for the peak cladding temperature of 400 °C and thermal decay constant of 0.023. The cladding oxide thicknesses as a function of temperature are presented in Figure 3–7. As seen in Figure 3–7, most of the cladding oxidation occurs in the first 20 years when cladding temperature is above 250 °C. This indicates that minimal-to-none cladding oxidation would occur when liquid phase water is in direct contact with the cladding material. For this reason, cladding corrosion in liquid phase water was not considered.

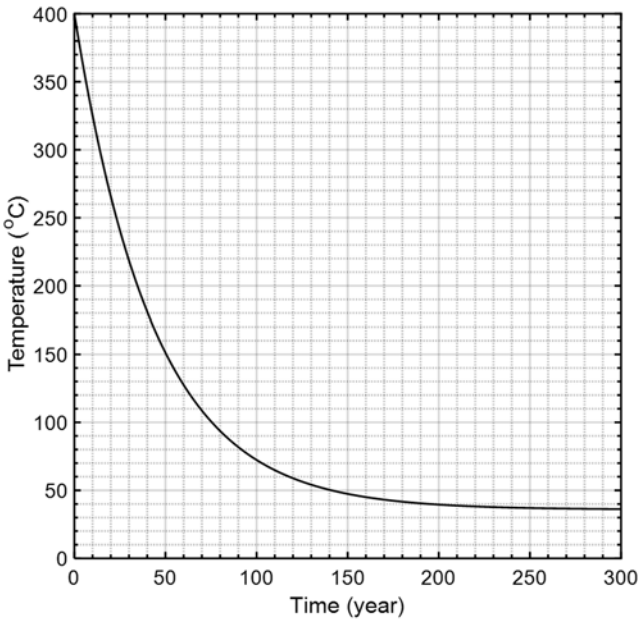

Figure 3–6. Temperature versus time profile

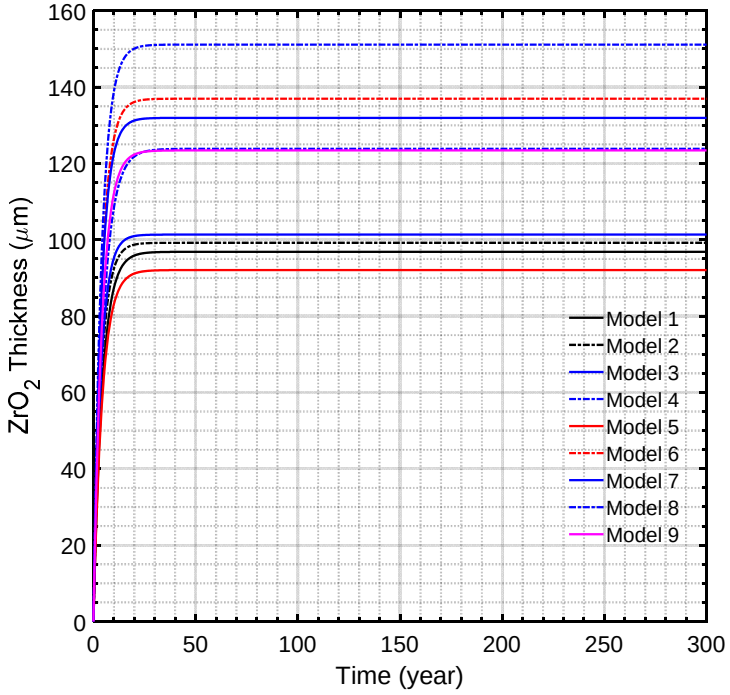

Cladding Oxide Thickness

Figure 3–7. Cladding Oxide Thickness for the Temperature-Time Profile in Figure 3–6

3.6 Corrosion Analysis

An integration model was used to quantitatively estimate extent of cladding oxidation and corrosion of various components inside the canister. The model is similar to the same as the one used in the CNWRA study, and was reconstructed using the code listing available in NRC (2013). The model accounts for both temporal and spatial variation of temperature their effects on cladding oxidation and corrosion of the subcomponents. The model integrated cladding oxidation, general corrosion of the internal components, and temperature distribution. The model inputs included cask parameters, fuel temperature at the time of loading cask internal volume, number of fuel assemblies, fuel rods per fuel assembly. Because the fuel and cladding temperatures are expected to vary spatially, the canister inside the cask volume is divided into five zones as detailed in Section 3.3.

The corrosion rates of various internal materials were estimated using the OLI Corrosion Analyzer Version 10.0. The corrosion rates were calculated for a range of hydrogen oxide concentration range of 0 to 2 M and temperature range of 25 to 120 °C. The corrosion rates were imported in the integration model and applied to the selected material. The corrosion rates were linearly interpolated if a temperature point during the time stepping did not precisely match the corrosion rate matrix imported in the integration model.

The integration model was executed assuming the storage time of 300 years. In each zone, it is assumed that the fuel and cladding temperatures are uniform. It is also assumed that the fuel temperature asymptotically approaches to ambient in 300 years. Initial fuel and cladding temperatures and volume

fraction of each zone are input to the model. Various cladding and canister model input parameters are listed in Table 3-6.

Table 3-6. Cladding, Fuel, and Canister Parameter Values Used in the Integration Model

Parameter	Values
Canister cavity volume	12 m^3
Number of fuel assemblies	21
Fuel rods per assembly	208 in 15 × 15 Babcock & Wilcox Fuel Assembly
Fuel rod length	3.9 m
Fuel rod outer diameter	10.92 mm
Number of zones	5
Cladding surface area	600 m^2
* x is assumed to be zero in the integration model.	

The integrated model calculates the extent of cladding oxidation, general corrosion thinning of the internal component materials, and amount of water needed to cause the oxidation.

4. CORROSION PROCESSES ANALYSIS

4.1 Cladding Oxidation

The integration model was simulated to calculate extent of cladding oxidation for the conditions listed in Table 4-1. The overall reactions leading to cladding oxidation and corresponding water consumption is following:

$$Zr + 2H_2O \rightarrow ZrO_2 + 2H_2 \quad (4–1)$$

Table 4-1. Cladding Oxidation Simulation Parameters in the Integrated Model	
Parameter	**Value**
Fuel and cladding initial temperature	Low- or high-end fuel and cladding initial temperature (as listed in Table 3-3)
Cladding alloy	Zircaloy-4, ZIRLO, and M5
Thermal decay constant	a equal to 0.023 or 0.064

The extent of cladding oxidation for peak cladding temperature of 302 °C and thermal decay constants of 0.023 and 0.064 is listed in Table 4-2. As listed, the maximum change in cladding thickness of 0.41 μm occurs for Zircaloy-4 in Zone 1. The changes in ZIRLO and M5 claddings are in submicron range.

The extent of cladding oxidation for peak cladding temperature of 400 °C and thermal decay constants of 0.023 and 0.064 is listed in Table 4-3. The extent of cladding oxidation is higher for higher initial peak cladding temperature. Zircaloy-4 could oxidize up to 12.8 μm in Zone 1 for the conditions of 400 °C initial temperature and thermal decay constant of 0.023; the extent of cladding oxidation is estimated to be 4.3 and 0.8 μm for ZIRLO and M5. The extent of cladding oxidation for the thermal decay constant of 0.064 is lower compared to 0.023. This is because the temperature decays faster, and cladding oxidation rates decrease with decreasing temperature.

Table 4-2. Extent of Cladding Oxidation due to Residual Water for Initial Peak Cladding Temperature of 302 °C						
Zone	**Cladding Thickness (μm)**					
	Thermal Decay Constant a=0.023			**Thermal Decay Constant a=0.064**		
	Zircaloy-4	**ZIRLO**	**M5**	**Zircaloy-4**	**ZIRLO**	**M5**
1	0.41	0.06	5.4×10^{-3}	0.15	2.0×10^{-2}	1.9×10^{-3}
2	4.5×10^{-2}	3.3×10^{-3}	2.2×10^{-2}	1.6×10^{-2}	1.2×10^{-3}	7.7×10^{-5}
3	3.2×10^{-3}	1.1×10^{-4}	4.5×10^{-6}	1.1×10^{-3}	4.1×10^{-5}	1.6×10^{-6}
4	1.3×10^{-4}	1.9×10^{-6}	4.1×10^{-8}	4.7×10^{-5}	6.7×10^{-7}	1.5×10^{-8}
5	2.7×10^{-6}	1.2×10^{-8}	1.2×10^{-10}	1.0×10^{-6}	4.38685E-09	4.4×10^{-11}

Table 4-3. Extent of Cladding Oxidation due to Residual Water for Initial Peak Cladding Temperature of 400 °C						
Zone	**Cladding Thickness (μm)**					
	Thermal Decay Constant a=0.023			**Thermal Decay Constant a=0.064**		
	Zircaloy-4	**ZIRLO**	**M5**	**Zircaloy-4**	**ZIRLO**	**M5**
1	12.8	4.3	0.80	4.6	1.5	0.30
2	2.5	0.55	7.4×10^{-2}	0.91	0.20	2.7×10^{-2}
3	0.40	5.0×10^{-2}	4.8×10^{-3}	0.14	1.8×10^{-2}	1.7×10^{-3}
4	4.1×10^{-2}	2.9×10^{-3}	1.9×10^{-4}	1.5×10^{-2}	1.1×10^{-3}	6.7×10^{-5}
5	4.5×10^{-3}	1.8×10^{-4}	7.5×10^{-6}	1.6×10^{-3}	6.3×10^{-5}	2.7×10^{-6}

The model was used to estimate minimum the amount of water needed to generate the oxidized cladding thicknesses listed in Table 4-2 and Table 4-3. The calculated values are listed in Table 4-4. The amount of water is highest for Zircaloy-4 for the peak initial temperature of 400 °C and thermal decay constant of 0.023, and is equal to 49.6 moles; this is equivalent to 900 mL at standard temperature and pressure.

Table 4-4. Minimum Amount of Water Needed to Oxidize Cladding for Different Peak Cladding Initial Temperature and Thermal Decay Constant			
Thermal Conditions	**Water Amount (Moles)**		
	Zircaloy-4	**ZIRLO**	**M5**
Peak Temperature = 302 °C, a = 0 0.023	1.40	0.20	0.02
Peak Temperature = 302 °C, a = 0 0.064	0.50	0.06	0.01
Peak Temperature = 400 °C, a = 0 0.023	49.6	14.8	2.5
Peak Temperature = 400 °C, a = 0 0.064	17.8	5.3	0.90

Shadow Corrosion Effects on Cladding

Galvanic corrosion in form of shadow corrosion could be caused by mismatch between clad and spacer-grid materials because the cladding is made of zirconium-based alloy, and spacer grids are made of Inconel alloys. In addition, the cladding material could be covered with a crud layer deposit during reactor operations. An electrochemical cell may form when water condenses in an opening between a fuel rod and a spacer grid and contacts both materials. The standard electrode potential for zirconium and ZrO_2 in aqueous solution at 25 °C is approximately −1.6 V_{SHE}, where the subscript SHE stands for standard hydrogen electrode. OLI simulations were conducted to calculate Pourbaix diagrams of zirconium in 0.01 and 2 M H2O2 solutions at 25 and 120 °C. Pourbaix diagrams for [H_2O_2] equal to 0.01 and 2.0 M at 25 °C are presented in Figure 4–1(a) and Figure 4–1 (b), respectively. In parallel, Pourbaix diagrams for [H_2O_2] equal to 0.01 and 2.0 M at 120 °C are presented in Figure 4–1(c) and Figure 4–1 (d),

respectively. As seen in the figures, zirconium is stable below -1.5 V_{SHE} at pH lower than 7. pH of the H_2O_2 solutions are expected to be lower than 7 because of H_2O_2 being an oxidizing species. Considering this -1.6 V_{SHE} is a reasonable value of corrosion potential for zirconium-based alloys in oxidizing solution containing H_2O_2.

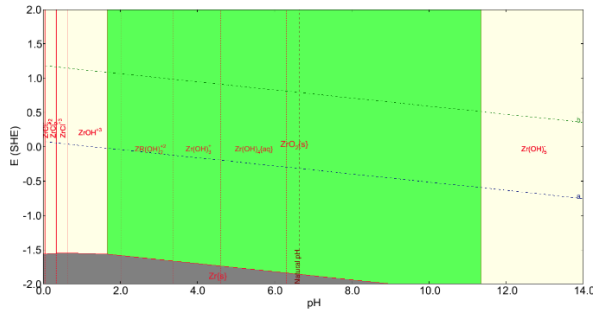

(a) T = 25 °C, [H_2O_2] = 0.01 M

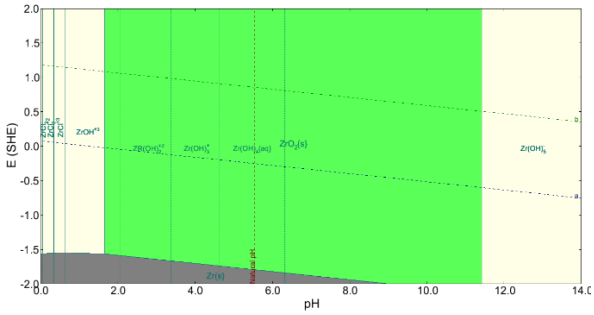

(b) T = 25 °C, [H_2O_2] = 2.0 M

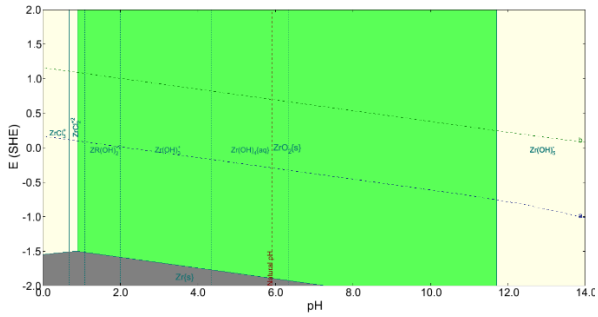

(c) T = 120 °C, [H_2O_2] = 0.01 M

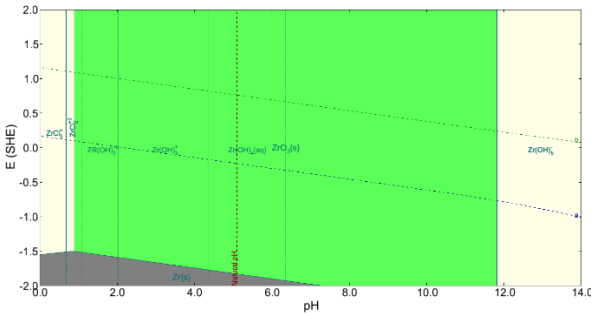

(d) T = 120 °C, [H_2O_2] = 2.0 M

Figure 4–1. Pourbaix Diagram of Zirconium in 0.01 and 2 M H2O2 Solutions at 25 and 120°C

The standard electrode potentials for chromium and nickel are equal to −0.74 and −0.23 V_{SHE}, respectively, at 25 °C. (Bard and Faulkner, 1980) When zirconium is electrically coupled with Ni-based alloys, it oxidizes into zirconium ion during the shadow corrosion and oxidizing species, such as oxygen and hydrogen peroxide in aqueous solution is reduced. Thus, the extent of damage would depend upon the oxidant amount present in the condensed water. The oxidation of zirconium and reduction of oxidizing species would occur according to the chemical reactions given by chemical Eqs. (4–2), (4–3), (4–4)

$$Zr \rightarrow Zr^{4+} + 4e^- \qquad (4–2)$$

$$H_2O_2 + 2e^- \rightarrow 2OH^- \qquad (4–3)$$

$$O_2 + 2H_2O + 4e^- \rightarrow 4OH^- \qquad (4–4)$$

According to the above equations, reduction of 1 mole of hydrogen peroxide would result in oxidation of 0.5 mole of zirconium. Similarly, reduction of 1 mole of oxygen would result in oxidation of 1.0 mole of zirconium. The amount of hydrogen peroxide and oxygen in 1 mole of 5 wt% H_2O_2 solution saturated with oxygen at 25 °C and 1 atm is 0.03 and 8.0×10^{-6} moles, respectively. The corresponding amount of zirconium that could be oxidized is 1.5×10^{-2} moles, which is equivalent to 1.37 g. The corresponding volume of the zirconium cladding material is approximately 0.25 cm^3. The depth of penetration on the cladding would depend upon the spread of the condensed water. However, it is expected that condensed water would not be localized and would spread over a large surface area. Therefore, even if shadow corrosion occurs, it is unlikely to result in through-wall cracks on the cladding.

4.2 Corrosion of Carbon Steel Components

Corrosion rates of generic carbon steel as a function of temperature and H_2O_2 concentration are presented in Figure 4–2. The corrosion rate data was used to estimate the loss of thickness of carbon steel components. The calculated loss of thicknesses as a function of H_2O_2 concentration are presented in Figure 4–3. The data in Figure 4–3 is for peak cladding initial temperatures of 302 and 400 °C and thermal decay constants of 0.023 and 0.064.

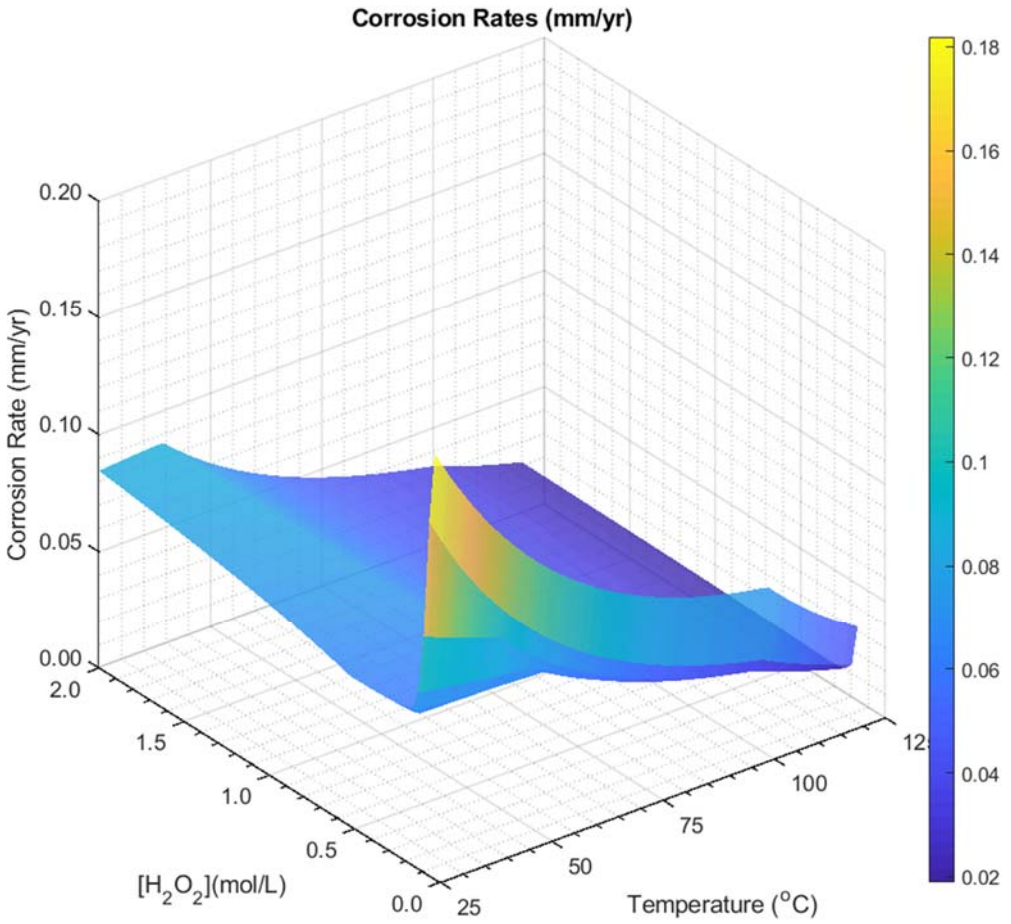

Figure 4–2. Carbon Steel Corrosion Rates as a Function of H_2O_2 Concentration and Temperature

The calculated loss of thicknesses, presented in Figure 4–3, indicate that most carbon steel components will experience extensive corrosion damage. As seen in the figure, the corrosion loss is more when peak initial temperature is lower and thermal decay constant is higher. This is because aqueous corrosion will occur when solution is in liquid phase, which is more likely at lower temperature than the higher temperatures. For a given peak initial temperature and larger thermal decay constant, the temperature zones in the canister will decay faster, hence the temperature will reach to aid the conditions of aqueous corrosion sooner; this is observed in Figure 4–3 (a) and Figure 4–3 (b). As seen in Figure 4–3 (b), the accumulated corrosion damage in the five zones if higher that the Figure 4–3 (a). Similarly, accumulated corrosion damage in the five zones of Figure 4–3 (d) is higher than the data in Figure 4–3 (c).

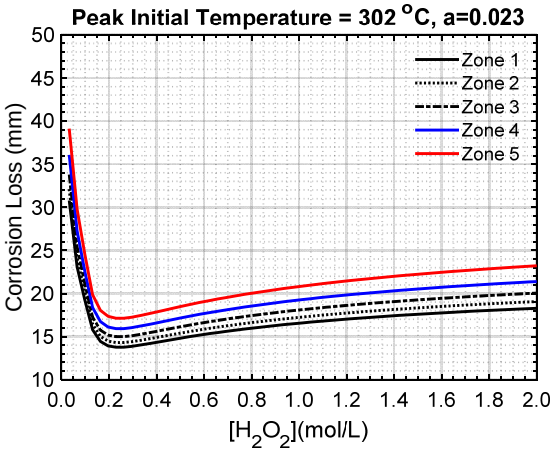

(a) Peak Initial Temperature = 302 °C, a = 0.023

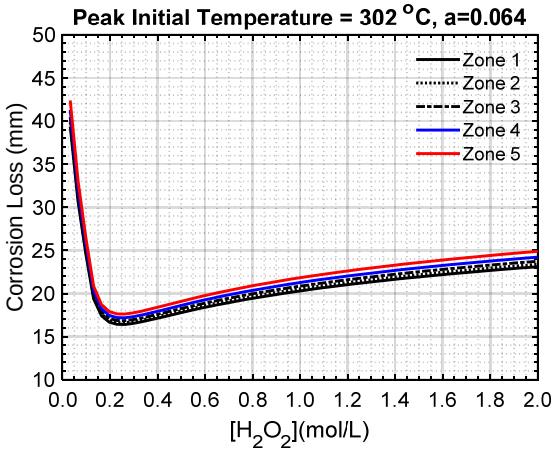

(b) Peak Initial Temperature = 302 °C, a = 0.023

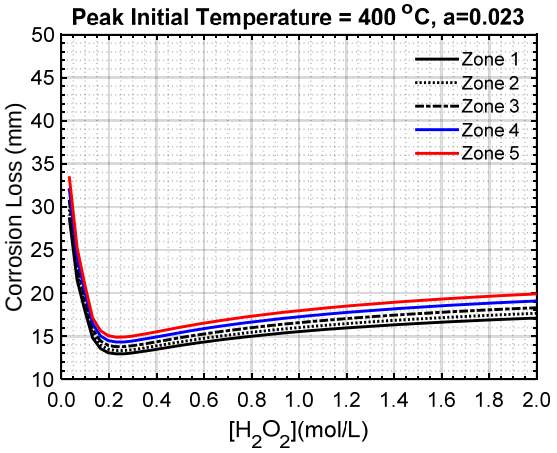

(c) Peak Initial Temperature = 400 °C, a = 0.023

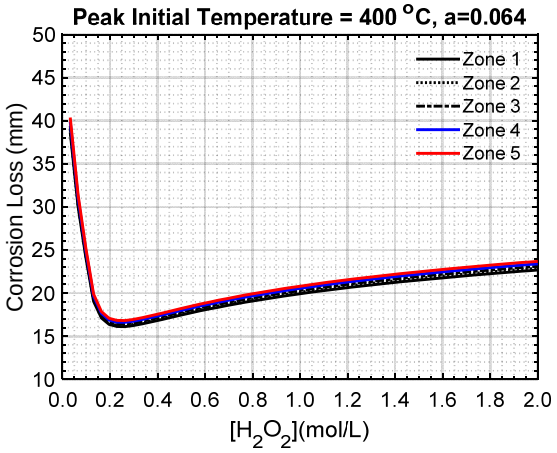

(d) Peak Initial Temperature = 400 °C, a = 0.023

Figure 4–3. Corrosion Loss of Carbon Steel in the Storage Canister Due to Residual Water for Peak Initial Temperatures of 302 and 400 °C and Thermal Decay Constants of 0.023 and 0.064

Prevalence of carbon steel fuel basket is limited, and only few storage canisters might have the fuel basket made of carbon steel. In addition, some transportation canister may also have the carbon steel fuel baskets. The carbon steel fuel baskets are most likely to be fabricated using 0.25-inch-thick plates. As per Figure 4–3, presence of unconstrained amount of water in the storage canister would result in extensive loss of basket structure, and hence, its ability to support the fuel in the analyzed configuration for criticality control could get compromised. A simplified calculation was conducted to determine the amount of water needed to corrode away a fuel basket for 24 PWR fuel assemblies. The basket was assumed to be located in a 70-inch inner diameter and 182-inch long cavity of the canister. The basket's largest plates are 65 in × 180 in. The widths of other basket plates were adjusted such that each fuel assembly cavity is 9 in × 9 in. The estimated mass of such fuel basket is 1.6 MT. With equivalent weight of carbon steel being 27.92 g/mole, it would need at least 56200 moles of residual water to corrode away the fuel basket; this is of course a theoretical minimum, much more than the theoretical minimum will be needed to corrode away a carbon steel fuel basket.

4.3 Corrosion of Stainless-Steel Components

Literature information suggests that most fuel baskets are made of austenitic stainless steels. Corrosion rates of a duplex and 304 stainless steels are presented in Figure 4–4(a) and Figure 4–4(b), respectively. As seen in the figure, corrosion rates of 304 SS are higher than the duplex SS.

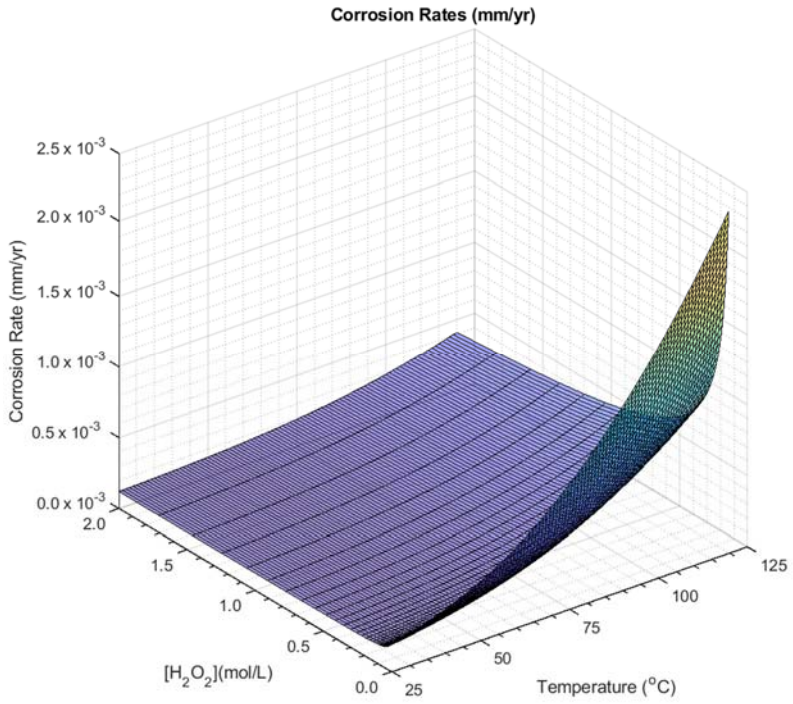

(a) Duplex Stainless Steel

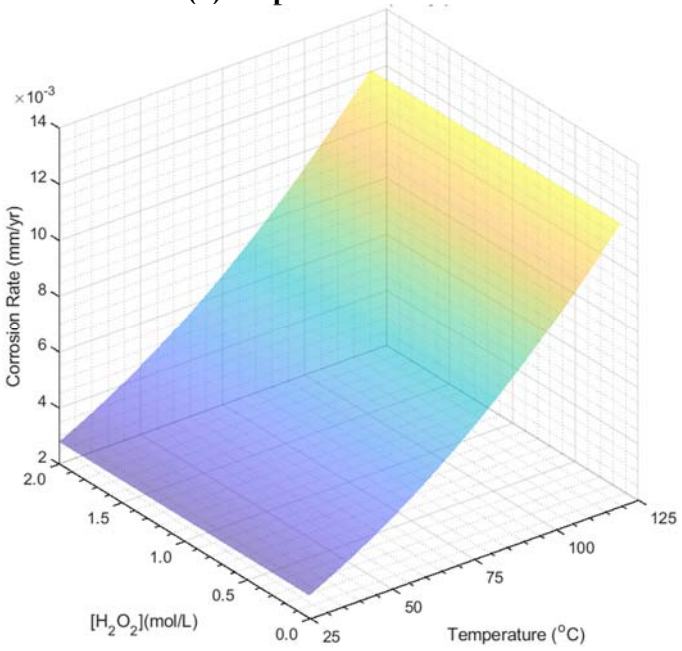

(b) 304 Stainless Steel

Figure 4–4. Corrosion Rates of (a) Duplex and (b) 304 Stainless Steel as a Function of H_2O_2 Concentration and Temperature.

The corrosion rate data was used to estimate the loss of material due to corrosion for a 300-year period. The corrosion loss in terms of thickness loss for duplex SS is presented in Figure 4–5. The loss of material is higher at the lower value of thermal decay constant but is independent of initial peak temperature; this is because temperature of the components and structure remain at higher temperatures for the lower value of the thermal decay constant, as a result, more corrosion occurs at elevated temperatures. It is also observed that more corrosion occurs at lower peroxide concentrations; this is due to complex interaction between passive film and peroxide amount in the solution. The passive film become more stable with increasing peroxide concentration.

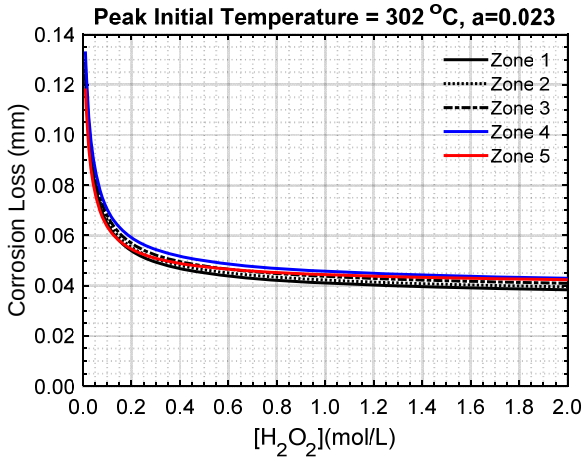

(a) Peak Initial Temperature = 302 °C, a = 0.023

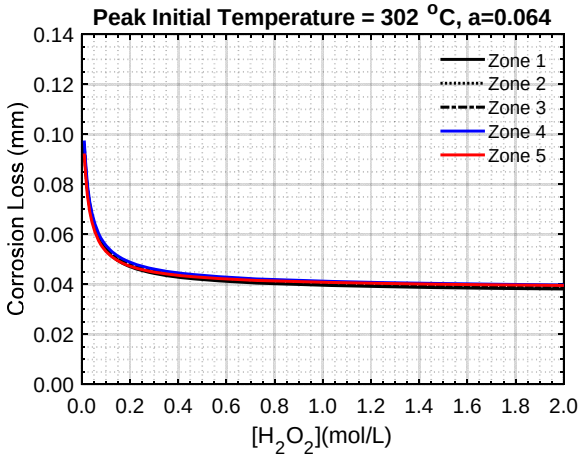

(b) Peak Initial Temperature = 302 °C, a = 0.023

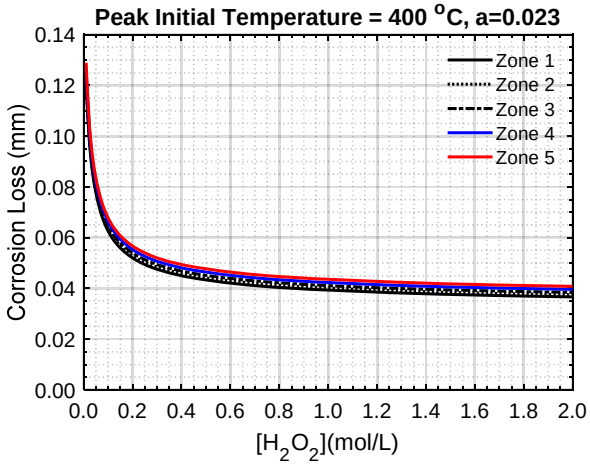

(c) Peak Initial Temperature = 400 °C, a = 0.023

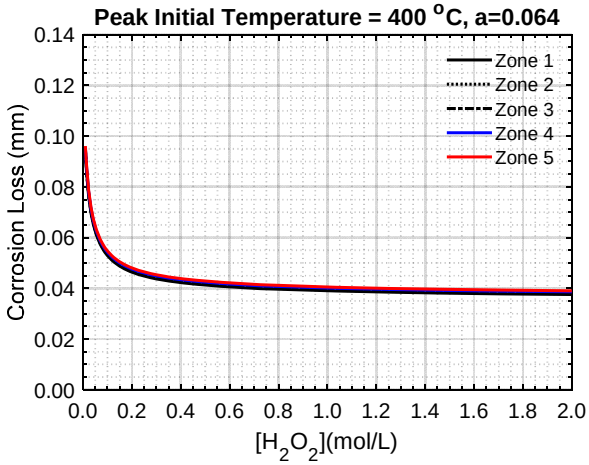

(d) Peak Initial Temperature = 400 °C, a = 0.023

Figure 4–5. Corrosion Loss of Duplex Stainless Steel in the Storage Canister Due to Residual Water for Peak Initial Temperatures of 302 and 400 °C and Thermal Decay Constants of 0.023 and 0.064

The corrosion loss in terms of thickness loss for 304 SS is presented in Figure 4–6. The loss of material for 304 SS is more than the duplex SS. This is because corrosion rates of 304 SS are higher almost by an order of magnitude compared to duplex SS. It is also noted that corrosion loss is independent of the H_2O_2 concentration. This indicates that corrosion mostly occurs in the passive dissolution range of oxidation reaction curve. It is also observed that the loss of material is higher at lower peak initial temperature.

This is because temperature of the components and structure reach the threshold for aqueous corrosion sooner when peak initial temperature is lower.

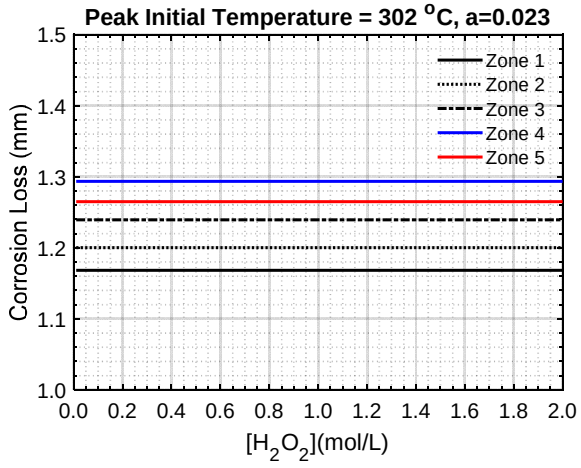

(a) Peak Initial Temperature = 302 °C, a = 0.023

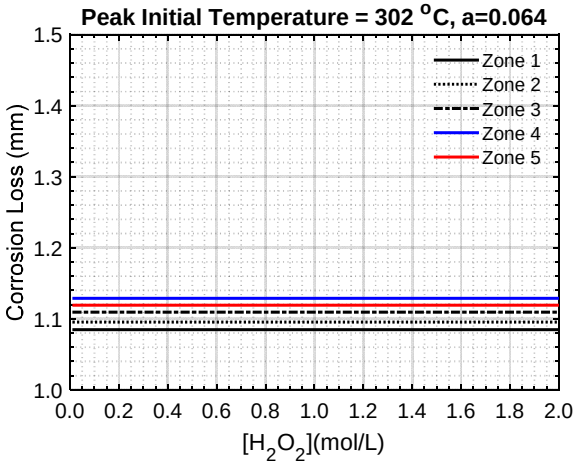

(b) Peak Initial Temperature = 302 °C, a = 0.023

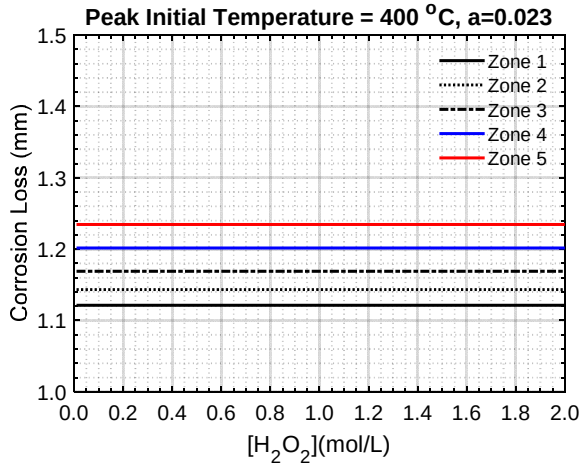

(c) Peak Initial Temperature = 400 °C, a = 0.023

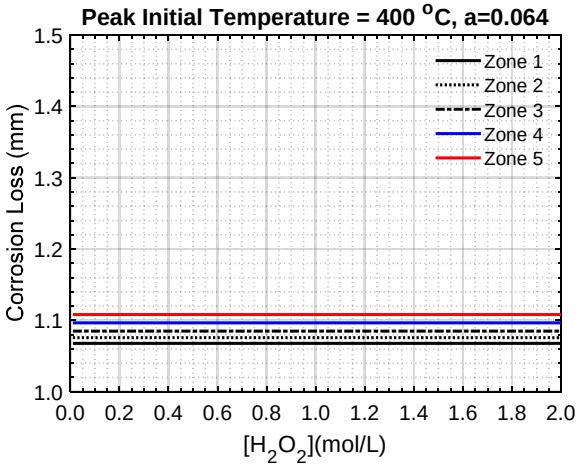

(d) Peak Initial Temperature = 400 °C, a = 0.023

Figure 4–6. Corrosion Loss of 304 Stainless Steel in the Storage Canister Due to Residual Water for Peak Initial Temperatures of 302 and 400 °C and Thermal Decay Constants of 0.023 and 0.064

Stainless steel fuel baskets are most widely used in the dry storage of spent nuclear fuel. The amount of water needed to cause the corrosion damage in Figure 4–5 and Figure 4–6 were calculated. The total amount of water for each combination of temperature and thermal decay constant is presented in Figure 4–7(a) and Figure 4–7(b) for duplex and 304 stainless steels, respectively. The water amounts for the five zones were added, and are represented as one curve as a function of H_2O_2 concentration for each combination of temperature and thermal decay constant. As seen in Figure 4–7(a) and Figure 4–7(b), the water amounts are highest for a given H_2O_2 concentration when peak initial temperature is 302 °C and thermal decay constant is 0.023; the next highest amounts are for peak initial temperature is 400 °C and thermal decay constant is 0.023. It is also noted that more water is consumed with the corrosion loss associated with 304 stainless steel compared to duplex stainless steel; this is consistent with the fact that

corrosion rates are higher for 304 SS, and more corrosion loss would occur to 304 SS fuel basket compared to duplex SS basket.

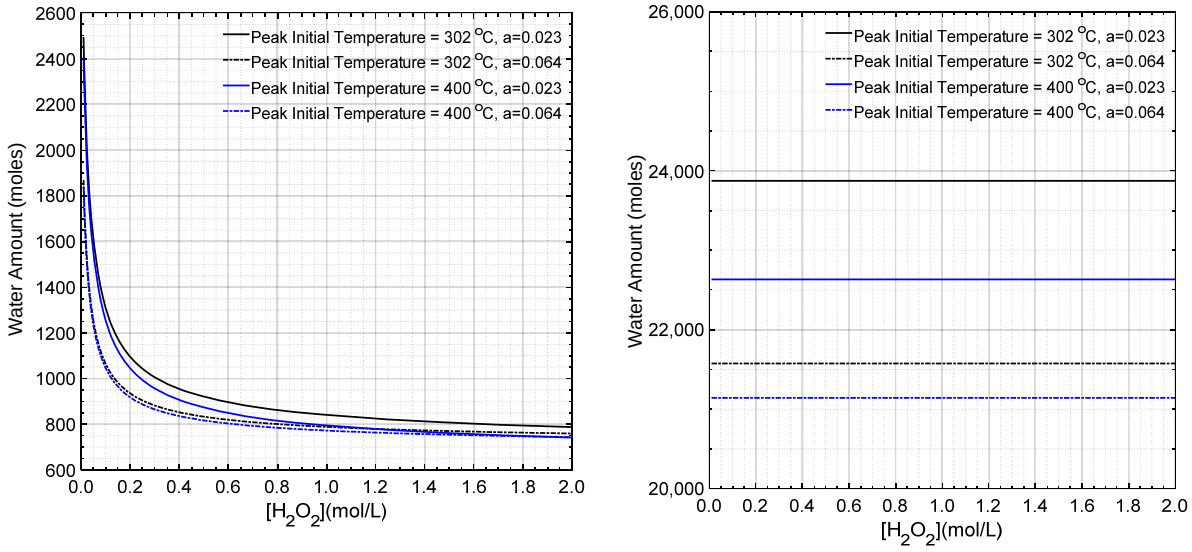

(a) Duplex Stainless Steel **(b) 304 Stainless Steel**

Figure 4–7. Water Amount Needed to Cause Corrosion Damage to Duplex and 304 Stainless Steel Fuel Baskets at Peak Initial Temperatures of 302 and 400 °C and Thermal Decay Constants of 0.023 and 0.064

4.4 Corrosion of Aluminum

Corrosion rate of commercially pure aluminum as a function of H_2O_2 concentration and temperature is presented in Figure 4–8. As seen in the figure, the corrosion rates peak at 2.0 M H_2O_2 and 120 °C.

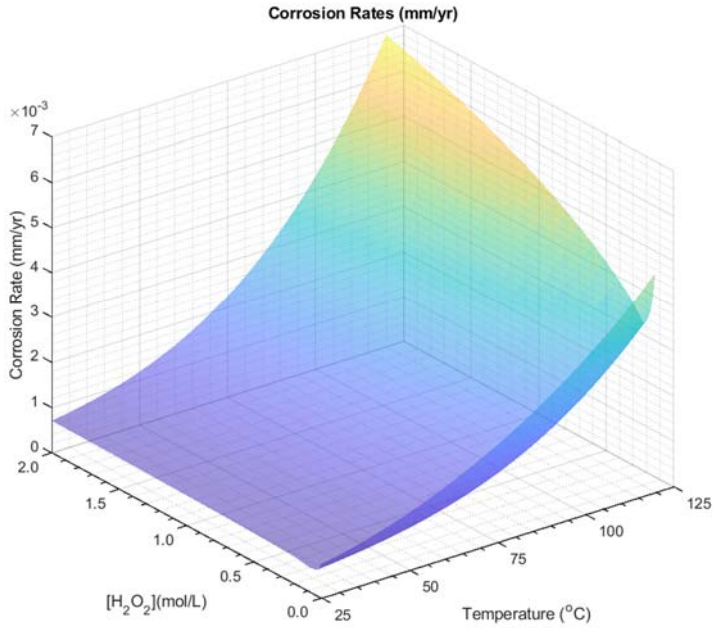

Figure 4–8. Corrosion Rates of Commercially Pure Aluminum as a Function of H_2O_2 Concentration and Temperature.

The corrosion rate data also demonstrate amphoteric characteristic of the material with increasing H_2O_2 concentration, i.e., the corrosion rate attain a minimum in the H_2O_2 concentration ranging from 0 to 2 M for a given temperature. The amphoteric behavior of the material becomes more pronounced with increasing temperature. The corrosion rate data in Figure 4–8 was used to estimate the loss of material due to corrosion. The corrosion damage in terms of thickness loss for commercially pure aluminum is presented in Figure 4–9. Similar to the other materials, the loss of material is higher at lower peak initial temperature for a given thermal decay constant. In addition, for a given peak initial temperature, the thickness loss is more for the lower value of the thermal decay constant. Regarding the effect of H_2O_2 concentration, the amphoteric characteristic of the material is also reflected in the thickness loss which dips to a minimum value around 0.1 M H_2O_2.

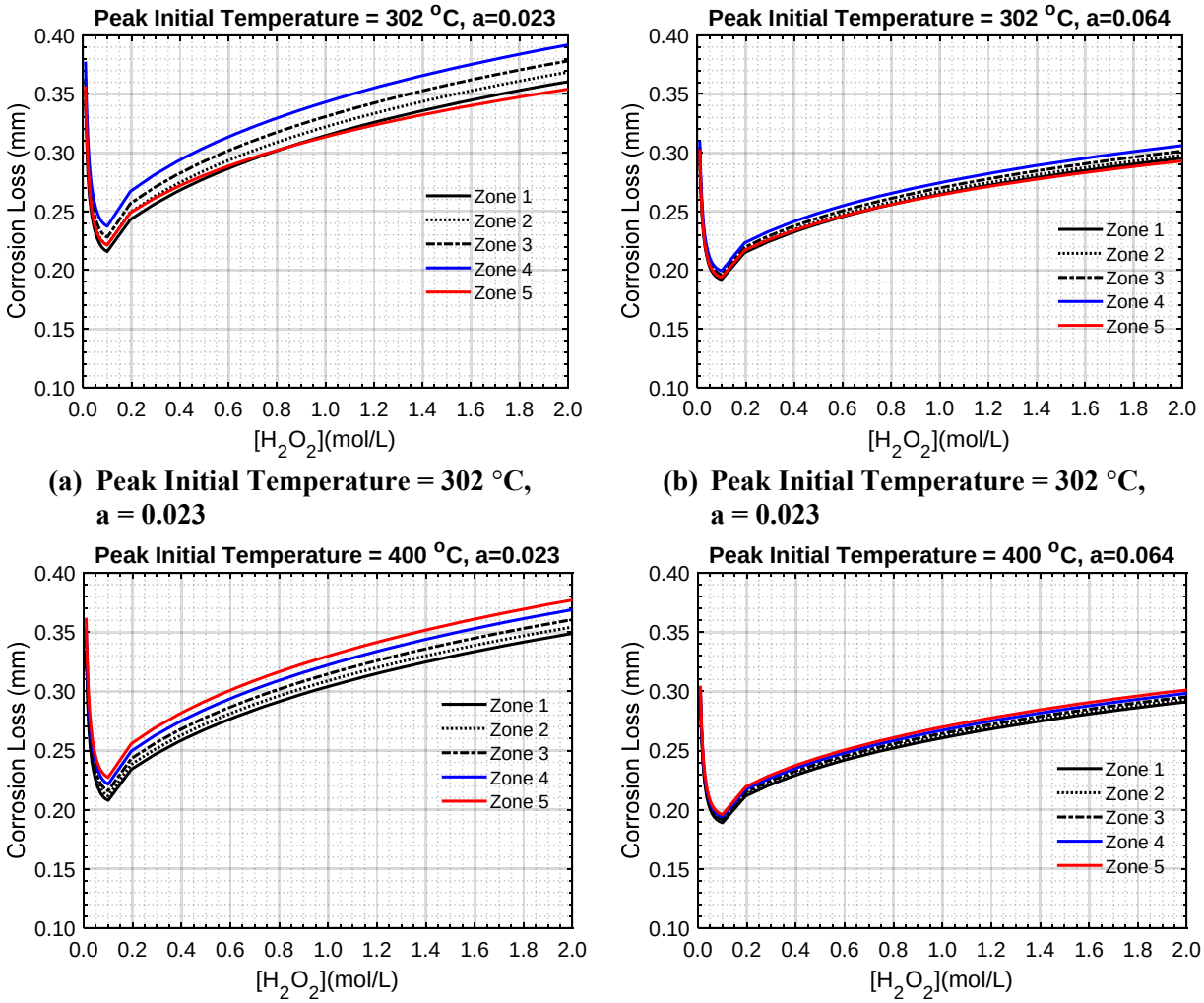

(a) Peak Initial Temperature = 302 °C, a = 0.023

(b) Peak Initial Temperature = 302 °C, a = 0.023

(c) Peak Initial Temperature = 400 °C, a = 0.023

(d) Peak Initial Temperature = 400 °C, a = 0.023

Figure 4–9. Corrosion Loss of Aluminum in the Storage Canister Due to Residual Water for Peak Initial Temperatures of 302 and 400 °C and Thermal Decay Constants of 0.023 and 0.064

Aluminum fuel baskets may have been used in some storage canister because their light weight. The amounts of water needed to cause the corrosion damage in Figure 4–9. The total amounts of water for each combination of temperature and thermal decay constant is presented in Figure 4–10. The water

amount pattern for aluminum is similar to other materials, i.e., the water amounts are highest for a given H_2O_2 concentration when peak initial temperature is 302 °C and thermal decay constant is 0.023; the next highest amounts are for peak initial temperature is 400 °C and thermal decay constant is 0.023. It is also noted that the magnitude of amounts of water for aluminum is similar to duplex stainless steel.

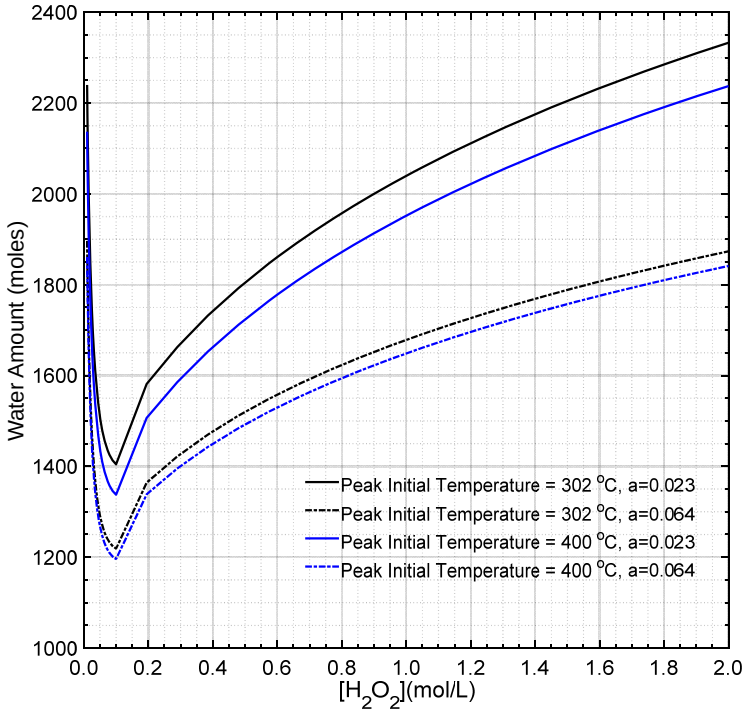

Figure 4–10. Water Amount Needed to Cause Corrosion Damage to Aluminum Fuel Baskets at Peak Initial Temperatures of 302 and 400 °C and Thermal Decay Constants of 0.023 and 0.064

4.5 Corrosion of Nickel Based Alloys

Nickel-based alloys are predominantly used in assembly hardware including guide tubes, spacer grids, and lower and upper end fittings. The guide tubes are fabricated using zirconium-based alloys. The other components are fabricated using one of the following materials: zirconium-based alloys, Inconel 718, Inconel 625, Inconel X-750, and stainless steel 304 L. These subcomponents are not expected to experience sustained external loads during passive dry storage except for their own weight. In the HI-STAR overpack, Inconel-718 is used to construct closure plate bolts and trunnion bolts, and nickel alloy X750 is used to construct seals. Nickel alloy 718 (ASME, 2007) is also used to construct the trunnion for the HI-TRAC transfer cask. Several nickel-based alloys are precipitation-hardened alloys that contain chromium to form a passive oxide film on the surface (Crook, 2005).

The corrosion rates of four nickel-based alloys were calculated: Alloy 625, Alloy 690, Alloy 825, and Alloy C276. These four alloys are expected to bound the composition range of the various nickel-based alloys that are used in fabrication of assembly hardware. The corrosion rate data is presented in Figure 4–11. As seen in the figure, the corrosion rates are mostly independent of H_2O_2 concentration, indicating that passive dissolution of these materials is expected to occur in the chemistry range with varying H_2O_2 concentrations. It is also noted that corrosion rates are highest for Alloy 690, and therefore bound and approximate other nickel-based alloys.

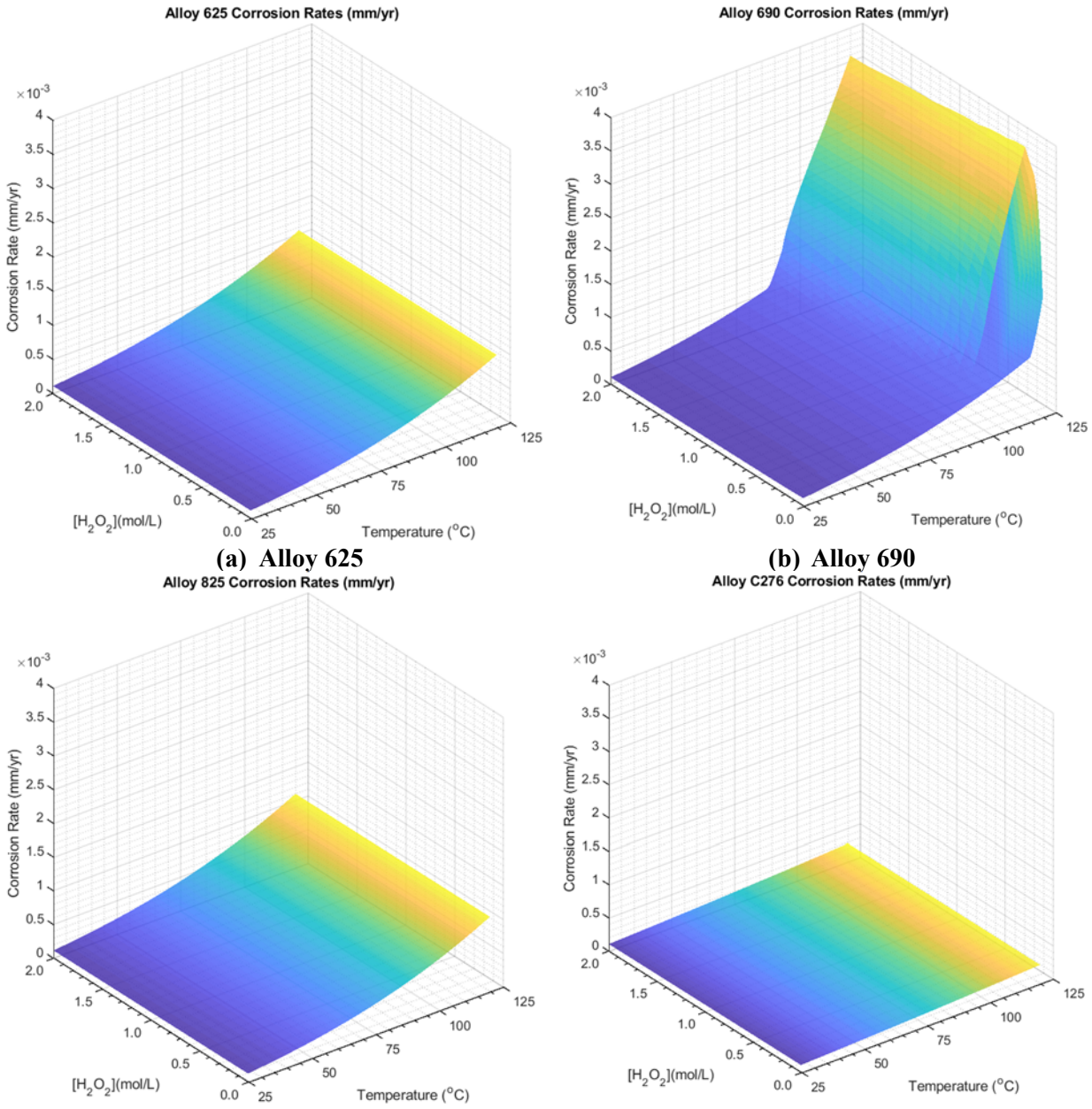

(a) Alloy 625 **(b) Alloy 690**

(c) Alloy 625 **(d) Alloy C276**

Figure 4–11. Corrosion Rates of the Four Nickel-Based Alloys as a Function of H_2O_2 Concentration and Temperature

Alloy 625 corrosion rate data was used to estimate the extent of corrosion loss for combinations of the peak initial temperatures of 302 and 400 °C and thermal decay constants of 0.023 and 0.064. The calculated corrosion damage in terms of thickness loss is presented in Figure 4–12. The maximum corrosion loss is no more than 100 µm for each combination of peak initial temperature and thermal decay constant. The water amounts needed to cause the corrosion damage are presented in Figure 4–13. As seen in the figure, the water amounts ranges from 65 to 108 moles for various combinations of peak initial temperature, thermal decay constant and H_2O_2 concentration.

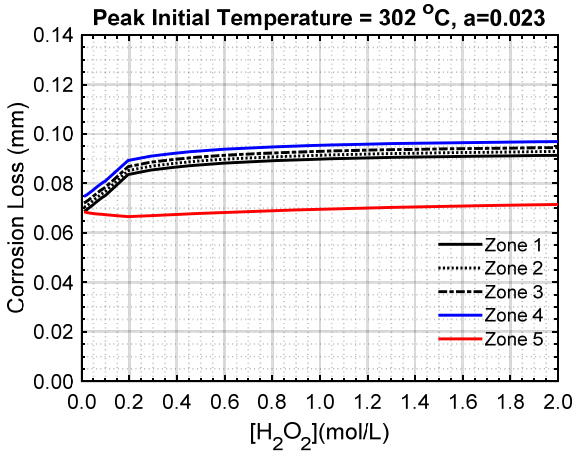

(a) Peak Initial Temperature = 302 °C, a = 0.023

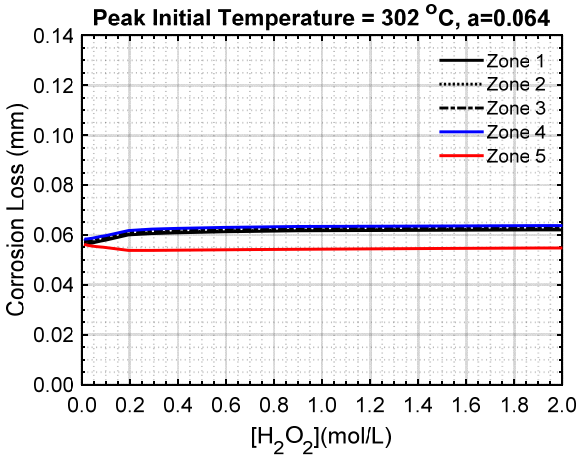

(b) Peak Initial Temperature = 302 °C, a = 0.023

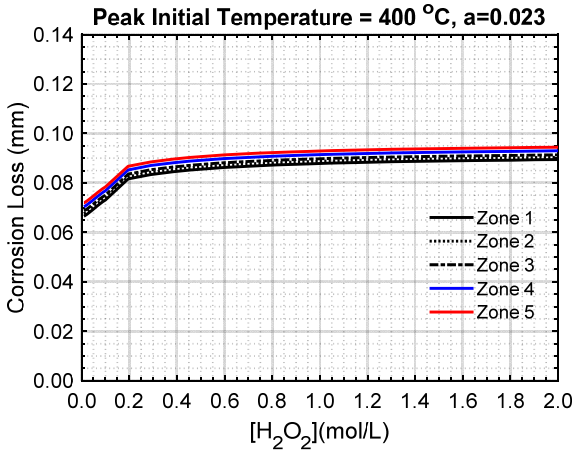

(c) Peak Initial Temperature = 400 °C, a = 0.023

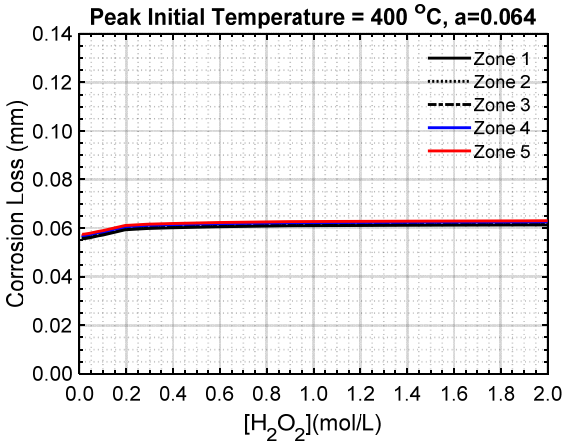

(d) Peak Initial Temperature = 400 °C, a = 0.023

Figure 4–12. Corrosion Loss of Alloy 625 in the Storage Canister Due to Residual Water for Peak Initial Temperatures of 302 and 400 °C and Thermal Decay Constants of 0.023 and 0.064

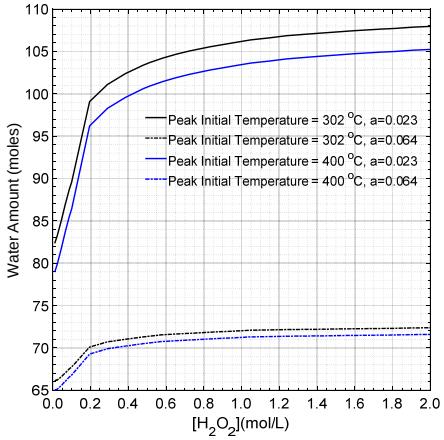

Figure 4–13. Water Amount Needed to Cause Corrosion Damage to Alloy 625 Components at Peak Initial Temperatures of 302 and 400 °C and Thermal Decay Constants of 0.023 and 0.064

4.6 Corrosion of BORAL

BORAL is a composite sheet formed by hot rolling consisting of (i) a core of uniformly mixed and distributed boron carbide and Aluminum 1100 particles and (ii) a surface cladding of Aluminum 1100 on both sides of the core, serving as a protective barrier as shown in Figure 4–14. The core typically contains between 35 and 65 wt% boron carbide, but is usually greater than 50 wt% (EPRI, 2012). The core of BORAL usually is not fully sintered and can have a porosity of 1 to 8 percent with varying degrees of interconnectivity, potentially allowing for water ingress into the core. The total thickness of BORAL is about 1.9–11.1 mm and cladding thicknesses are typically between 250–380 μm on each side (EPRI, 2009).

Aluminum 1100 is essentially pure aluminum with a minimum 99 percent aluminum content by weight (EPRI, 2009). The BORAL outer barrier is fabricated from an Aluminum 1100 cladding that will be in more direct contact with the residual water than the core and, consequently, will likely degrade more than the core.

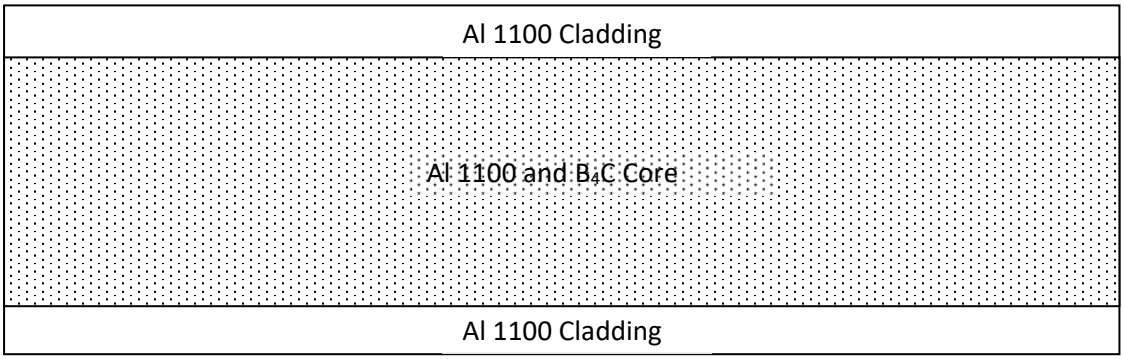

Figure 4–14. . Schematic Cross-Section of BORAL Showing the Cladding Structure and the Core

AAR Cargo Systems (1987) examined general corrosion of BORAL, which is likely the slowest corrosion process. In AAR Cargo Systems (1987), the general corrosion rate for Aluminum 1100 was determined to be 4.6 to 8.1 μm/yr at 20 to 66 °C in borated spent fuel pool water. One BORAL manufacturer reported a maximum corrosion rate of 7.2 μm/yr for two sides exposed at 38 °C for 1 year in PWR and BWR waters, which is 3.6 μm/yr for each cladding side (EPRI, 2009). The literature corrosion rate data is consistent with the corrosion rate dada in Figure 4–8. For a storage canister with 24 PWR fuel assemblies, there would be 96 BORAL panels for criticality control. Assuming 9 in × 9 in × 180 in, total surface area of the 96 BORAL panel would approximately equal to 2×10^6 cm^2. Amount of water needed to corrode away 250 μm of the Al-cladding on both sides of the each panel would be require approximately 5000 moles of residual water.

Blister Formation: Blister formation degrades BORAL because it affects the physical form of the material. Blisters have been observed under the cladding of both surveillance coupons and some spent-fuel storage racks containing BORAL in both BWR and PWR SFPs since BORAL was first used in 1964 (EPRI, 2012). The blisters typically occur in localized areas as a result of gas pressure buildup leading to (i) separation of aluminum cladding from the underlying boron carbide aluminum composite and (ii) physical outward deformation. The diameters of blisters range from less than 1 cm up to tens of centimeters, and heights vary from less than about 0.1 cm up to several centimeters.

It is commonly surmised that blistering occurs when SFP water migrates into the boron carbide aluminum composite core either along the cut edges or through penetrations caused by pitting corrosion of the aluminum cladding. Water reacts with aluminum in the BORAL core forming hydrogen gas and solid corrosion products, such as boehmite (γ-AlOOH), gibbsite [Al(OH)3] or alumina (Al_2O_3). The volume expansion resulting from the solid corrosion products is believed to seal off pore spaces in the BORAL core (EPRI, 2009). As corrosion proceeds, hydrogen gas builds up inside the sealed pore spaces, which ultimately results in the formation of blisters. In general, it is observed that blisters are more likely to occur in coupons subjected to BWR water than those exposed to PWR water. Furthermore, tests showed that blisters become larger at higher radiation levels as a result of hydrogen production from radiation. For the spent fuel storage module, the industry uses EPRI (2012) vent holes to relieve the H_2 pressure buildup in the shroud to prevent bulging.

Blistering of the BORAL panels during dry storage is still a topic of research, and is beyond the scope of this report. It is therefore assumed that no residual water is consumed in blistering of the BORAL panels.

4.7 Corrosion of Borated Stainless Steel

These borated stainless steel alloys have been used in the nuclear industry for spent fuel storage and transportation racks and cask baskets, control rods, burnable poison, and shielding to control the reactivity of SNF (Wasinger, 1993). Borated stainless steel is reported to be highly stable for wet and dry storage service environments (EPRI, 2009).

Type 304 borated stainless steels are similar in composition to regular Type 304 stainless steels except that they contain boron, which provides a much higher thermal neutron absorption cross section than unborated austenitic stainless steels. The solubility of boron in stainless steel is low, and the production of alloys with more than 2.25 wt% boron content is difficult. ASTM A887–89 (ASTM International, 2009) defines eight types (304B and 304B1–304B7) of borated stainless steels with boron concentrations from 0.2 to 2.25 wt%. Requirements for the chemical composition of borated stainless steel for nuclear application are provided in ASTM International (2009).

Increasing boron content increases thermal neutron absorption capabilities, hardness, tensile strength, and yield strength, but decreases tensile ductility, impact toughness, and corrosion resistance (CRS Holdings, Inc., 2003). For each type of borated stainless steel with the same chemical composition, ASTM A887–89 (ASTM International, 2009) specifies two grades (A and B) defined by the uniformity of boron dispersion within the matrix. According to ASTM A887–89, Grade A corresponds to the near optimal boron dispersion, while Grade B corresponds to a less-than-optimal dispersion of the boron. The difference in uniformity of boron dispersion leads to differences in material ductility and toughness. ASTM A887–89 specifies that Grade A has increased impact and tensile testing requirements compared to those for Grade B.

Historically, the only way to meet the Grade A requirements was to produce material with a powder metallurgy technique. Conventional cast-and-wrought metallurgical practice can reach Grade B properties; however, ASTM International does not preclude using powder metallurgy techniques in the supply of Grade B materials. EPRI (2009) lists products conforming to ASTM A887–89 (ASTM International, 2009) specifications from two suppliers: NeutroSorb®, NeutroSorb Plus®, or Micro-Melt® NeutroSorb (Carpenter Powder Products, USA) and Neutronit® (Bohler Bleche GmbH, Austria).

Borated stainless steel alloys solidify as primary austenite with a terminal eutectic constituent, which has the form (Fe, Cr)2B, with the exact composition dependent on the initial boron level (Goldschmidt, 1971). The austenite matrix is a ductile phase, and the dispersed secondary phase is a comparatively brittle compound. With the same chemical composition, the metallurgical structure differs depending on fabrication techniques. For products that use the powder metallurgy technique, the secondary phase is

finer and more uniformly distributed compared to that used by the cast-and-wrought process. The Grade B material produced by the powder metallurgy technique has a consistent microstructure along the cross section compared to that produced by the cast-and-wrought technique. The difference in microstructure usually leads to a difference in mechanical properties and corrosion resistance. Powder metallurgy material tends to have higher corrosion resistance and easily meets ASTM A887–89 (ASTM International, 2009) specification requirements.

The borated stainless steel thickness varies depending on whether enriched B-10 is used in fabrication. If the alloy is produced with boron enriched to a level of 95 percent in the B-10 isotope, a thickness of 2.5 mm is sufficient to achieve the desired B-10 areal density. However, if the alloy is produced with natural boron, approximately 12.5-mm-thick plates are required to provide adequate reactivity control.

Borated stainless steel is a type of stainless steel that can experience typical degradation modes, including general corrosion, localized corrosion, SCC, MIC, intergranular corrosion, and galvanic corrosion. In an SNF storage application, general and localized corrosion are expected to be the dominant degradation mechanisms of borated stainless steel. One form of localized corrosion is intergranular corrosion, which is a preferential attack at the grain boundaries of a stainless steel. It is generally the result of sensitization. In borated stainless steel, the formation of chromium-rich secondary phase (Fe, Cr)2B particles could lead to intergranular corrosion. EPRI (2009, 1992) reported that borated stainless steel is susceptible to intergranular corrosion in acidic environments with pH <2; therefore, this degradation mechanism is not likely during storage. Furthermore, stainless steels are typically manufactured with carbon content less than 0.03 percent to minimize the potential for intergranular corrosion.

General corrosion degrades borated stainless steel because it leads to material thinning. Borated stainless steel passivates in water because a chromium oxide film forms, which makes the material highly corrosion resistant. Under normal conditions, general corrosion occurs slowly by metal dissolution through the oxide film. General corrosion has been shown to occur for borated stainless steels (He and Pabalan, 2012; He et al., 2012). He and Pabalan (2012) and He et al. (2012) examined borated stainless steel in water with a boron concentration of 2,600 ppm; the studies examined Type 304B4 stainless steel at 60, 75, and 90 °C for 9 months. The studies showed that the general corrosion rates of 304B4 were hundreds of nm/yr with no clear dependence on temperature.

Bailey and Johnson (1983) examined the corrosion rate of Type 304 stainless steel in high-purity water. They reported a corrosion rate of Type 304 stainless steel less than 0.25 μm/yr. A corrosion data survey lists a corrosion rate of Type 304 SS in very dilute boric acid-water environment of less than 50 μm/yr (Bailey and Johnson, 1983).

The corrosion rate was estimated by considering that the stainless-steel corrosion rate typically decreases with time as the oxide film evolves (Subramanian, 2007). Based on this and the experimental data, the corrosion rate is assumed to be about 1-14 μm/yr, same as the corrosion rates of 304 SS in Figure 4-4(b). With this corrosion rates, the borated SS would thin similar to the data in Figure 4-6, and the amount of water needed to corrode away the material would be approximately double of the data in Figure 4-7(b).

4.8 Localized Corrosion

Localized corrosion either in the form of pitting or crevice corrosion would occur only when an aqueous solution is present. Localized corrosion would initiate when the corrosion potential is greater than the repassivation potential (Shukla, et al., 2008). Corrosion and repassivation potentials for carbon steel, SS304, pure aluminum, and nickel-based Alloy 600 series in 0.01 and 2 M H_2O_2 aqueous solutions saturated with oxygen at 25, 75, and 125 °C were calculated using the OLI Software. The corrosion and

repassivation potential data for the 0.01 and 2 M H_2O_2 aqueous solutions are listed in Table 4-5 and Table 4-6, respectively. As per the data listed in Table 4-5 and Table 4-6, the corrosion potentials are lower than the repassivation potential for the four metals in the 0.01 and 2 M H_2O_2 aqueous solutions. These data indicate that localized corrosion of the structural component materials is not likely due to residual water.

Localized damage to the neutron-absorbing material BORAL in the form of blistering has been observed. A postulated mechanism for blister formation is based on water entering the material during fuel loading operations from the SNF pool to a dry storage cask. Water could enter through open porosity at the edges. During dry storage at elevated temperatures, water contacting the internal surfaces of interconnected pores causes internal corrosion and produces Al_2O_3 and hydrogen gas. The volume change associated with Al_2O_3 formation causes the pores to close, thus entrapping hydrogen and water in the core of the neutron-absorbing material. Subsequent formation of hydrogen and/or heating of trapped hydrogen cause internal pressure buildup and material deformation. As temperature decreases during extended storage, this process decreases, which decreases the likelihood to affect the basket structural integrity for very long-term storage.

Table 4-5. Calculated Corrosion and Repassivation Potentials for Carbon Steel, SS304, Pure Aluminum, and Alloy 625 in 0.01 M H_2O_2 Aqueous Solution Saturated with Oxygen at 25, 75, and 125 °C

Temperature °C	Corrosion Potential (mV_{SHE})				Repassivation Potential (mV_{SHE})			
	Carbon Steel	SS304	Pure Aluminum	Alloy 600	Carbon Steel	SS304	Pure Aluminum	Alloy 600
25	−470	302	−185	338	>2000	>2000	>2000	>2000
75	−496	265	−406	316	>2000	>2000	>2000	>2000
125	−499	261	−628	322	>2000	>2000	>2000	>2000

Table 4-6. Calculated Corrosion and Repassivation Potentials for Carbon Steel, SS304, Pure Aluminum, and Alloy 625 in 2 M H_2O_2 Aqueous Solution Saturated with Oxygen at 25, 75, and 125 °C

Temperature °C	Corrosion Potential (mV_{SHE})				Repassivation Potential (mV_{SHE})			
	Carbon steel	SS304	Aluminum	Alloy 600	Carbon Steel	SS304	Pure Aluminum	Alloy 600
25	−477	302	−170	357	>2000	>2000	>2000	>2000
75	−498	265	−402	298	>2000	>2000	>2000	>2000
125	−500	263	−626	300	>2000	>2000	>2000	>2000

Regarding borated stainless steels, if localized corrosion occurred in the form of pitting, the rates would be much higher than the general corrosion rates. In the tests by He and Pabalan (2012) conducted in water with a boron concentration of 2,600 ppm at 60, 75, and 90 °C for 9 months with 304B4, pitting corrosion was observed at 90 °C, but not at 60 and 75 °C. The pitting density was about 10 pits per 30 cm^2. Localized corrosion may also occur in the form of crevice corrosion if crevices exist. From the limited experimental evidence, localized corrosion will occur, but more information on the design is needed to predict the amount of degradation. Pitting corrosion of the borated stainless steels in the residual waters of storage canisters needs to be further investigated.

4.9 Galvanic Corrosion

Galvanic corrosion in the form of shadow corrosion between Inconel alloy and zirconium-based cladding materials has been addressed in the previous discussion. In this section galvanic corrosion between a combination of carbon steel, stainless steel, and pure aluminum is discussed, and the extent of damage due to galvanic couples of carbon and stainless steels, carbon steel and pure aluminum, and stainless steel and pure aluminum is estimated. Galvanic corrosion would occur when two dissimilar metals are in physical contact and a layer of aqueous solution covers both the metals. Oxidation of the active (i.e., less noble) metal would occur, whereas reduction reactions would take place at the nobler metal surface. Nobility of a metal in a metal couple can be determined by analyzing the corrosion potential values. Corrosion potential values of various alloys in flowing seawater that are readily available (Shukla, 2008) are used to infer the relative nobility of the canister materials during extended storage. Table 4-7 lists the corrosion potentials of carbon steel, various stainless steel types, and aluminum-based alloys.

The alloy or metal with lower corrosion potential value in a metal couple would undergo oxidation. Therefore, if galvanic corrosion is occurring between carbon steel and any type of stainless steel, carbon steel would undergo oxidation. Similarly, an aluminum alloy would undergo oxidation when galvanic corrosion occurs between an aluminum alloy and stainless steel, and carbon steel would undergo oxidation in a galvanic couple between carbon steel and stainless steel.

The dissolution of iron will be the predominant chemical reaction in the oxidation of the carbon steel and is expressed by chemical Eq. (4–5)

$$Fe \rightarrow Fe^{2+} + 2e^{-} \quad (4–5)$$

Similarly, the dissolution of aluminum will be the predominant chemical reaction in the oxidation of an aluminum-based alloy and is expressed by chemical Eq. (4–6)

$$Al \rightarrow Al^{3+} + 3e^{-} \quad (4–6)$$

Table 4-7. Corrosion Potentials of Various Alloys in Flowing Seawater

Alloy	Corrosion Potential (mV_{SHE})
Stainless Steel: Type 316 and 317	100 to 240
Stainless Steel: Types 302, 304, 321, 347	120 to 170
Carbon Steel	−159 to −360
Aluminum Alloys	−460 to −660

The extent of these reactions would depend upon the availability of the oxidizing species in the condensed water. As discussed in the previous section, the amount of hydrogen peroxide and oxygen in 1 mole of 5 wt% H_2O_2 solution saturated with oxygen at 25 °C and 1 atm is 0.03 and 8.0×10^{-6} moles, respectively. This amount of oxidizing species could oxidize 3.0×10^{-2} moles of iron and 2.0×10^{-2} moles of aluminum. This corresponds to 1.7 g of iron and 0.54 g of aluminum. These values are small compared to the mass of materials used in building a storage canister. This analysis indicates that while galvanic corrosion may occur inside a canister due to residual water, the extent of damage to structural materials would depend on configurational contact between two dissimilar materials.

5. SUMMARY AND CONCLUSIONS

The impact of residual water on canister internals, with a focus on the fuel basket, oxidation of the cladding, and various cladding hardware materials such as spacer grids. It is assumed that the canister is loaded with intact fuel, i.e., fuel is not exposed to the canister internal environment. Radiolysis of the residual water is expected to yield the oxidizing species such as hydrogen peroxide and oxygen. Based on analysis of the residual water radiolysis, it was assumed that hydrogen peroxide concentration range between 0 to 2 M. Corrosion rates of various canister internal materials were estimated using a commercially available software., and the rates were estimated for a range of temperature and hydrogen peroxide concentration. An "integration model," was used to couple the temperature variations with the corrosion rates, and extent of corrosion of various internal components were estimated.

This study provided the following findings of corrosion/oxidation of the cladding and canister internals for the period of 300 years under decaying temperature conditions and with unlimited water:

- General corrosion is expected to be dominant degradation mechanism, localized corrosion either in form of pitting or crevice corrosion is unlikely.
- Maximum loss of cladding thickness due to general corrosion is not expected to exceed 13 μm. The maximum loss of cladding would occur for Zircaloy-4 in a canister with peak cladding temperature of 400 °C. The maximum cladding thickness loss will be confined to no more than 20% of the total fuel rods. The cladding thickness loss to rods located away from the peak temperature of 400 °C is expected to be less than 3 μm. This material corrosion loss is effectively limited, regardless of the amount of residual water, due to the temperature drop-off in time with concomitant extremely low corrosion kinetics.
- Both stainless steel and nickel-based alloys and not expected to experience significant loss of thickness due to general corrosion. Maximum loss of thicknesses to the stainless steel and nickel-based components is expected to be on the order of 1 and 0.1 mm, respectively. This material corrosion loss is effectively limited, regardless of the amount of residual water, due to the temperature drop-off in time with concomitant extremely low corrosion kinetics.
- Corrosion of aluminum-based components could lead up to 0.4 mm loss of thickness. Most BORAL plates have sheathing layers of aluminum sheets which are 250-μm (0.25-mm) thick. This indicates that BORAL plates may experience extensive loss of thickness of the aluminum sheathing where liquid phase residual water accumulates. The role of passive films that would reduce the corrosion rate of aluminum in the canister internal environment did not account for a complex oxide such as gibbsite/bayerite and boehmite mixtures.
- Corrosion of carbons-steel based components could be significant, and loss of thickness could exceed components' manufactured dimensions. However, carbon steel is not commonly used in the storage canisters, but may have been used in transportation canisters.

The findings are generic and are primarily dependent on the thermal conditions of the packaged SNF in a canister. The water amount data in Chapter 4 is compiled for the sake of developing an understanding on totality of the residual water for the specific canister considered in this study. The specific amount of water needed to sustain cladding oxidation, and general corrosion of fuel basket and nickel-based alloy assembly hardware in the above is listed in Table 5-1. The listed data indicate that total amount of water needed has a weak independence on the peak cladding temperature, but stronger dependence on the thermal decay constant. For example, the amount of water needed to oxidize Zircaloy-4 cladding, duplex stainless steel fuel basket, Ni-based alloys assembly hardware at peak cladding temperatures of 302 and 400 °C with thermal decay constants of 0.023 differ only by 30 moles, whereas water amounts differ by almost 600 moles for a given peak initial temperature but different thermal decay constant. This analysis also show that more water is consumed with lower value of the thermal decay constant; this observation is consistent with the fact that internal components will remain at higher temperatures for longer periods

with the lower value of the thermal decay constant than with the higher value of the thermal decay constant.

The amount of water with the aluminum fuel basket is comparable to the one with the duplex stainless steel. However, the amount of water with the 304 stainless steel is an order of magnitude higher than the other two. This is because 304 SS general corrosion rates are higher than duplex SS and Al1100.

Table 5-1. Estimated Water Amount to Cause the Extent of Corrosion of the Zircaloy-4 Cladding, Fuel Basket, and Ni-Based Hardware

Thermal Conditions	Water Amount (moles)		
	Cladding, Duplex Stainless Steel Fuel Basket, Ni-Based Alloy Hardware	Cladding, 304 Stainless Steel Fuel Basket, Ni-Based Alloy Hardware	Cladding, Aluminum Fuel Basket, Ni-Based Alloy Hardware
Peak Temperature = 302 °C, a = 0 0.023	2600	23,980	2440
Peak Temperature = 302 °C, a = 0 0.064	1940	21,650	1970
Peak Temperature = 400 °C, a = 0 0.023	2570	22,800	2390
Peak Temperature = 400 °C, a = 0 0.064	1930	21,230	1950

It is noted that the water amounts listed in Table 5-1 are theoretical limits, and are not constrained by the steps of the vacuum drying process and canister cavity volume after packaging of the fuel. For example, the maximum amount of 23,980 moles in Table 5-1 is approximately equal to 430 L at standard temperature and pressure, whereas in the fuel loading and drying steps, residual water is first drained out which eliminates most of the residual water. In addition, the thickness loss data due to corrosion in Chapter 4 is generic and can be used to estimate the extent when the residual water amounts are lower than the theoretical limit. For example, if the water amounts are few moles, but persist as liquid phase in contact with a given component for the storage duration, the thickness loss would be primarily dependent on the chemistry and component's thermal conditions.

Overall, an analysis of the corrosion rates and integration model results provide following insights. General corrosion of the internal components is the dominant mechanism for consumption of the residual water. Further, even with the general corrosion, the internal components are not expected to degrade to a point where their structural integrity is compromised. However, if there are carbon steel components, extensive general corrosion could occur resulting in loss of material thickness that could exceed the initial condition when fuel was loaded. Finally, and oxidation of the cladding is expected to be minimal even with unlimited amount of the water.

6. REFERENCES

AAR Cargo Systems. "BORAL Neutron Absorbing/Shielding Material." Report No.624. Detroit, Michigan: Brooks and Perkins, Inc. 1987.

ASME. Boiler and Pressure Vessel (B&PV) Code, Section III, "Rules for Construction of Nuclear Facility Components," Division 1, Subsection NB, "Class 1 Components," and Subsection NC, "Class 2 Components"; American Society of Mechanical Engineers. 2007.

ASTM International. "Standard Specification for Borated Stainless Steel Plate, Sheet, and Strip for Nuclear Application." ASTM A887–89. West Conshohocken, Pennsylvania: ASTM International. 2009.

Bailey, W.J. and A.B. Johnson. "Wet Storage Integrity Update." PNL–4726. Richland, Washington: Pacific Northwest Laboratory. 1983.

Bard, A.J. and L.R. Faulkner. Electrochemical Methods, Fundamentals and Applications. New York City, New York: John Wiley & Sons. 1980.

Billot, P., P. Beslu, A. Giodano, and J. Thomazel. "Development of a Mechanistic Model To Assess the External Corrosion of the Zircaloy Claddings in PWRs." Presented at the Zirconium in the Nuclear Industry: 8th International Symposium. L.F.P. Van Swam and C.M. Eucken, eds. ASTM STP 1023. Philadelphia, Pennsylvania: ASTM International. pp. 165–184. 1989.

Bryan, C.R., S.G. Durbin, E. Lindgren, A.G. Ilgen, T.J. Montoya, T. Dewers, D. Fascitelli. "SNL Contribution: Consequence Analysis for Moisture Remaining in Dry Storage Canisters After Drying," Sandia National Laboratory, SAND2019-8532 R, 2019a.

Bryan, C.R., R.L. Jarek, C. Flores, and E. Leonard. Analysis of Gas Samples Taken from the High Burnup Demonstration Cask. SAND2019-2281. Sandia National Laboratories, Albuquerque, NM. 2019b.

Bryan, C., R.L. Jarek, C. Flores, and E. Leonard. "Analysis of Gas Samples Collected from the DOE High Burnup Demonstration Cask". International High-Level Radioactive Waste Management Conference 2019. Knoxville, TN, American Nuclear Society. 2019c.

Bryan, C.R., S.G. Durbin, E. Lindgren, A.G. Ilgen, T.J. Montoya, T. Dewers, D. Fascitelli. "SNL Contribution: Consequence Analysis for Moisture Remaining in Dry Storage Canisters After Drying," Sandia National Laboratory, SAND2019-8532 R, 2019c

Buxton, G. V., C.L. Greenstock, W.P. Helman, A.B. Ross, "Critical Review of Rate Constants for Reactions of Hydrated Electrons, Hydrogen Atoms and Hydroxyl Radicals (•OH/•O−) in Aqueous Solution." J. Phys. Chem. Ref. Data, Vol. 17, pp. 513-886. 1988.

Cheng, B.C., D. Smith, E. Armstrong, K. Tunage, and G. Bond. "Water Chemistry and Fuel Performance in LWRs." Proceedings of the 2000 International Topical Meeting on Light Water Reactor Fuel Performance, Park City, Utah, April 10–13, 2000. Published on CD-ROM. La Grange Park, Illinois: American Nuclear Society. 2000.

CNWRA. Extended Storage and Transportation: Evaluation of Drying Adequacy. Authors: H. Jung, P. Shukla, T. Ahn, L. Tipton, K. Das, X. He, and D. Basu, San Antonio, Texas: Center for Nuclear Waste Regulatory Analyses. 2013.

Cox, B. "Oxidation of Zirconium and its Alloys." Advances in Corrosion Science and Technology. M. Fontana and R.W. Staehle, eds. New York City, New York: Plenum Press. 1976.

Cox, B. "Degradation of Zirconium Alloys in Water Cooled Reactors." Presented at the 3rd International Symposium on Environmental Degradation of Materials in Nuclear Power Systems-Water Reactors. Warrendale, Pennsylvania: The Metallurgical Society. pp. 65–76. 1988.

Crook, P. "Corrosion of Nickel and Nickel-Base Alloys, Corrosion: Materials." Vol 13B. ASM Handbook. ASM International. pp. 228–251. 2005.

CRS Holdings, Inc. "Micro-Melt® NeutroSorb® Plus Alloys Data." Wilmington, Delaware: CRS Holdings, Inc. 2003.

Daalgard, S.B. "Long-Term Corrosion and Hydriding of Zircaloy-4 Fuel Clad in Commercial Pressurized Water Reactors With Forced Convective Heat Transfer." Extended Abstracts of the Electrochemical Society. Vol. 76-1, No. 31. p. 82. 1976.

d'Entremont, A. L., R.L. Kesterson, and R.L. Sindelar. "Evaluation of Hydrogen Generation in High Burnup Demonstration Dry Storage Cask," SRNL-STI-2020-00268. Aiken, South Carolina: Savannah River National Laboratory. 2020.

Dyce, I.H. "Corrosion of Zircaloy Fuel Cladding: The Influence of High Heat Fluxes." Nuclear Engineering. Vol. 9, No. 98. pp. 253–255. 1964.

EPRI. "Borated Stainless Steel Application in Spent Fuel Storage Racks." TR–100784. Palo Alto, California: Electrical Power Research Institute. 1992.

EPRI. "Spent Fuel Transportation Applications—Assessment of Cladding Performance A Synthesis Report-Final Report." EPRI-TR-1015048. Palo Alto, California: Electric Power Research Institute. 2007.

EPRI. Handbook of Neutron Absorber Materials for Spent Nuclear Fuel Transportation and Storage Application. 2009 Edition. Palo Alto, California: Electric Power Research Institute. 2009.

EPRI. "Strategy for Managing the Long-Term Use of BORAL® in Spent Fuel Storage Pools." Technical Report No. 1025204. Palo Alto, California: Electric Power Research Institute. July 2012.

Garde, A.M. "Enhancement of Aqueous Corrosion of Zircaloy-4 Due to Hydride Precipitation at the Metal-Oxide Interface." Proceedings of the Zirconium in the Nuclear Industry: 9th International Symposium. C.M. Eucken and A.M. Garde, eds. ASTM STP 1132. West Conshohocken, Pennsylvania: ASTM International. pp. 566–594. 1991.

Garzarolli, F., W. Jung, H. Schoenfeld, A.M. Garde, G.W. Parry, and P.G. Smerd. "Waterside Corrosion of Zircaloy Fuel Rods." EPRI NP–2789. Palo Alto, California: Electric Power Research Institute. 1982.

Stehle, H., W. Kaden, and R. Manzel. "External Corrosion of Cladding in PWRS." Nuclear Engineering and Design. Vol. 33. pp. 155–169. 1975.

Ghali, E. Corrosion Resistance of Aluminum and Magnesium Alloys: Understanding, Performance and Testing. Hoboken, New Jersey: John Wiley & Sons, Inc. 2010.

Goldschmidt, H.J. "Effect of Boron Additions to Austenitic Stainless Steels Part II, Solubility of Boron in 18 Percent Cr, 15 Percent Ni Austenitic Steel." Journal of the Iron and Steel Institute. Vol. 6. p. 910. 1971.

He, X. and R. Pabalan. "Update on Laboratory Corrosion Experiments—Key Regulatory and Technical Issues." San Antonio, Texas: Center for Nuclear Waste Regulatory Analyses. 2012.

He, X., T. Ahn, and T. Sippel. "Corrosion of Borated Stainless Steel in Water and Humid Air." Proceedings of the CORROSION 2012 Conference, Corrosion in Nuclear Systems Symposium, Salt Lake City, Utah, March 11–15, 2012. Paper No. 01142. Houston, Texas: NACE International. 2012.

Hillner, E. "Corrosion of Zirconium-Base Alloys: An Overview." Presented at the Zirconium in the Nuclear Industry—3rd International Symposium. A.L. Lowe, Jr. and G.W. Parry, eds. ASTM STP 633. Philadelphia, Pennsylvania: ASTM International. pp. 211–235. 1977.

Hillner, E., D.G. Franklin, and J.D. Smee. "The Corrosion of Zircaloy-Clad Fuel Assemblies in a Geological Repository Environment." WAPD–3173. West Miffin, Pennsylvania: Bettis Atomic Power Laboratory. 1994.

Jensen, B.J. and D.J. Richmond. "Thermal Analysis of High Decay Heat Loading Strategies in the MAGNASTOR System," Pacific Northwest National Laboratory, PNNL-XXXX, 2019.

Knight, T. "Experimental Determination and Modeling of Used Fuel Drying by Vacuum and Gas Circulation for Dry Cask Storage," Nuclear Energy University Programs, Project No. 14-7730. U.S. Department of Energy, 2018

Knight, T.W., J. Khan, T. Farouk, and J. Tulenko. "Experimental Determination of Used Fuel Vacuum Drying Using a Mock Fuel Assembly". International High-Level Radioactive Waste Management Conference, April 9-13, 2017. Charlotte, NC, American Nuclear Society. 2017.

Knoll, R.W. and E.R. Gilbert, "Evaluation of Cover Gas Impurities and Their Effects on the Dry Storage of LWR Spent Fuel," PNL 6365, November 1987.

Lousada C. and M. Jonsson, "Kinetics, Mechanism, and Activation Energy of H2O2 Decomposition on the Surface of ZrO_2," The Journal of Physical Chemistry C. Vol. 114, No. 25, pp. 11202–11208, 2010.

Mardon, J.P., D. Charquet, and J. Senevant. "Influence of Composition and Fabrication Process on Out-of-Pile and In-Pile-Properties of M57 Alloy." Proceedings of the Zirconium in the Nuclear Industry: 12th International Symposium. G.P. Sabol and G.T. Moan, eds. ASTM STP 1354. West Conshohocken, Pennsylvania: ASTM International. pp. 505–524. 2000.

NUREG/CR-6846, "Air Oxidation Kinetics for Zr-Based Alloys," U.S. Nuclear Regulatory Commission," ML16112A084, Argonne National Laboratory, 2004.

NRC, "Scientific Notebook # 1098E: Development of an Integration Model to Evaluate Effect of Residual Water on Fuel and Cladding Oxidation," ML13144A148, Washington, DC: U.S. Nuclear Regulatory Commission. 2013.

NRC. NUREG–2214, "Managing Aging Processes In Storage (MAPS) Report." Washington, DC: U.S. Nuclear Regulatory Commission. July 2019.

OLI Analyzer Version 10.0, OLI Systems Inc. Parsippany, NJ, 2020.

Peters, H.R. "Improved Characterization of Aqueous Corrosion Kinetics of Zircaloy-4." Presented at the Zirconium in the Nuclear Industry: 6th International Symposium. D.G. Franklin and R.B. Adamson, eds. ASTM STP 824. Philadelphia, Pennsylvania: ASTM International. pp. 507–518. 1984.

Rothman, A.J. "Potential Corrosion and Degradation Mechanisms of Zircaloy Cladding on Spent Nuclear in a Tuff Repository." UCID–20172. Livermore, California: Lawrence Livermore National Laboratory. 1984.

Sindelar, R.L., A.J. Duncan, M.E. Dupont, P.-S. Lam, M.R. Louthan, Jr., and T.E. Skidmore. NUREG/CR–7116, "Materials Aging Issues and Aging Management for Extended Storage and Transportation of Spent Nuclear Fuel." Washington, DC: U.S. Nuclear Regulatory Commission. 2011.

Shukla, P.K., R. Pabalan, T. Ahn, L. Yang, X. He, and H. Jung. "Cathodic Capacity of Alloy 22 in the Potential Yucca Mountain Repository Environment." Proceedings of the CORROSION 2008 Conference, Corrosion in Nuclear Systems Symposium, New Orleans, Louisiana, March 16–20, 2008. Paper No. 08583. Houston, Texas: NACE International. 2008.

Shukla, P. "Thermodynamics of Corrosion and Potentiometric Methods for Measuring Localized Corrosion." Techniques for Corrosion Monitoring. L. Yang, ed. Cambridge, England: Woodhead Publishing. pp. 156–186. 2008.

Shukla, P., R. Sindelar, P.-S. Lam "Consequence Analysis of Residual Water in a Storage Canister." SRNL–STI–2019–00495. Aiken, South Carolina: Savannah River National Laboratory. 2019.

Subramanian, K.H. "Life Estimation of Transfer Lines for Tank Farm Closure Performance Assessment." WSRC–STI–2007–00460. Aiken, South Carolina: Savannah River National Laboratory. 2007.

Suzuki, M. and S. Kawasaki. "Oxidation of Zircaloy Cladding in Air." Journal of Nuclear Materials. Vol. 140. pp. 32–43. 1986.

Teague, M.C., S.J. Saltzstein, B. Hanson, K. Sorenson, and G. Freeze, "Gap Analysis to Guide DOE R&D in Supporting Extended Storage and Transportation of Spent Nuclear Fuel: An FY2019 Assessment," SAND-2019-15479R, DOI 10.2172/1592862. 2019.

Van der Linde, A. "Calculation of the Safe Life Time Expectancy of Zirconium Alloy Canning in the Fuel Elements of the NERO Reaction." RCN Report 41. Petten, The Netherlands: Reactor Centrum. 1965.

Van Swam, L.F., G.M. Bain, W.C. Dey, D.D. Davis, and H. Heckermann. "BWR and PWR Fuel Performance at High Burnup." Proceedings of the 1997 International Topical Meeting on LWR

Performance, Portland, Oregon, March 2–6, 1997. La Grange Park, Illinois: American Nuclear Society. pp. 3–10. 1997.

Wasinger, K. "High Density Spent Fuel Storage in Spain-Capacity for the Entire Life." Nuclear Plant Journal. Vol. 4. p. 46. 1993.